Università degli Studi di Padova

Dipartimento di Fisica e Astronomia
Corso di Laurea Magistrale in Astronomia

A data-driven model for the cosmic merger rate density of compact binaries

Master Degree Thesis

Candidate:
Filippo Santoliquido

Supervisor:
Prof.ssa Michela Mapelli

Co-supervisor:
Dott. Nicola Giacobbo

Anno Accademico 2018-2019

The art of research is the sensitivity to decide when a useful and necessary simplification has become an obfuscating oversimplification.

Richard Levins

Abstract

The eleven gravitational wave detections reported so far provide crucial insights on compact binary astrophysics. One key open question in this field is to understand the cosmic evolution of gravitational wave sources. In my thesis, I have developed a new data-driven method to predict the cosmic merger rate density (MRD) of compact object binaries. In particular, I have combined catalogues of merging compact objects from population-synthesis simulations with a data-driven cosmological evolution model, including the observational cosmic star formation rate density (SFRD) (Madau and Dickinson, 2014) and two metallicity evolution models (Rafelski et al., 2012; De Cia et al., 2018). Double neutron star MRD depends mainly on the adopted isolated binary evolution prescriptions, while binary black hole MRD is basically driven by metallicity evolution. Each MRD evolution with redshift shows an increasing trend up to a peak and a consequent decrease. The peak position can be shifted with respect to the SFRD maximum, depending on the delay time distributions. My model has been compared with two previous works. The first (Neijssel et al., 2019) obtained the cosmic MRD including a redshift-independent metallicity spread. The second work (Mapelli and Giacobbo, 2018) is based on a completely numerical model, where cosmic star formation rate and metallicity evolution come from the Illustris cosmological simulation. My model is in good agreement with these previous works and is significantly faster (a factor of ≥ 10) than purely numerical models.

Contents

Chapter 1

Introduction

The first direct gravitational wave (GW) detection - GW150914 - revolutionised the theoretical understandings of compact binaries. Astrophysicists learnt about the existence of binary balck holes (BBHs) that inspiral and merge within an Hubble time (Abbott et al., 2016). The inferred masses demonstrate that relatively heavy ($M_{BH} > 25M_{\odot}$) stellar black hole (BH) can form in nature. Since 2015 until 2017, during the first and the second observing run, the LIGO-Virgo collaboration (LVC) searched for new events and now the astrophysics community can refer to a catalogue that contains 11 merging compact binaries (The LIGO Scientific Collaboration et al., 2018). The inferred parameters that describe this population are listed in table 1.1. This set of ten BBHs and one double neutron star (DNS) posed new questions regarding the formation channels of these detected binaries.

These objects possess a wide range of physical properties. For example, the lightest BBH so far detected is GW170608 with an inferred final mass of $17.8^{+3.2}_{-0.7}$ $M_{\odot}$; while GW170729 is the heaviest, having a final mass equal to $80.3^{+14.6}_{-10.2}$ $M_{\odot}$. Furthermore, it is the most distant, since it merged at redshift $z = 0.48^{+0.19}_{-0.20}$. In April 2019, LVC began the third observing run (03), which will last one year. Therefore, several other GW detections are expected to enrich the above-mentioned catalogue. Each observing run has experienced improvements on sensitivity and these lead to an enhancement of the observing horizon. For instance, Advanced LIGO at design sensitivity can observe two merging black holes with masses $(30 + 30)M_{\odot}$ out to a cosmological redshift equal to $z \sim 1$ (Abbott et al., 2018). The observatory network will search for mergers in the entire Universe. Hence, it is essential to predict the double compact object (DCO) merger rate density (MRD) across cosmic time.

I developed a model that evaluates the MRD from merging DCO catalogues obtained with population-synthesis simulations. Isolated binary evolution was performed using MOBSE, which is an updated version of the widely used binary population synthesis code BSE (Giacobbo et al., 2018b). In chapter 3, I will carefully describe the input parameters, the involved physical processes and the results of the population-synthesis simulations. I placed merging DCO obtained from isolated binary evolution in a cosmological context. The star formation rate reported in Madau and Dickinson (2014) and two metallicities evolution models (Rafelski et al.,

Event	$\frac{m_1}{M_\odot}$	$\frac{m_1}{M_\odot}$	$\frac{M_{chirp}}{M_\odot}$	χ_{eff}	$\frac{M_f}{M_\odot}$	$\frac{d_L}{\mathrm{Mpc}}$	z	$\frac{\Delta\Omega}{\mathrm{deg}^2}$
GW150914	$35.6^{+4.8}_{-3.0}$	$30.6^{+3.0}_{-4.4}$	$28.6^{+1.6}_{-1.5}$	$-0.01^{+0.12}_{-0.13}$	$63.1^{+3.3}_{-3.0}$	430^{+150}_{-170}	$0.09^{+0.03}_{-0.03}$	180
GW151012	$23.3^{+14.0}_{-5.5}$	$13.6^{+4.1}_{-4.8}$	$15.2^{+2.0}_{-1.1}$	$0.04^{+0.28}_{-0.19}$	$35.7^{+9.9}_{-3.8}$	1060^{+540}_{-480}	$0.21^{+0.09}_{-0.09}$	1555
GW151226	$13.7^{+8.8}_{-3.2}$	$7.7^{+2.2}_{-2.6}$	$8.9^{+0.3}_{-0.3}$	$0.18^{+0.20}_{-0.12}$	$20.5^{+6.4}_{-1.5}$	440^{+180}_{-190}	$0.09^{0.04}_{-0.04}$	1033
GW170104	$31.0^{+7.2}_{-5.6}$	$20.1^{+4.9}_{-4.5}$	$21.5^{+2.1}_{-1.7}$	$-0.04^{+0.17}_{-0.20}$	$49.1^{+5.2}_{-3.9}$	960^{+430}_{-410}	$0.19^{+0.07}_{-0.08}$	924
GW170608	$10.9^{+5.3}_{-1.7}$	$7.6^{+1.3}_{-2.1}$	$7.9^{+0.2}_{-0.2}$	$0.03^{+0.19}_{-0.07}$	$17.8^{+3.2}_{-0.7}$	320^{+120}_{-110}	$0.07^{+0.02}_{-0.02}$	396
GW170729	$50.6^{+16.6}_{-10.2}$	$34.3^{+9.1}_{-10.1}$	$35.7^{+6.5}_{-4.7}$	$0.36^{+0.21}_{-0.25}$	$80.3^{+14.6}_{-10.2}$	2750^{+1350}_{-1320}	$0.48^{+0.19}_{-0.20}$	1033
GW170809	$35.2^{+8.3}_{-6.0}$	$23.8^{+5.2}_{-5.1}$	$25.0^{+2.1}_{-1.6}$	$0.07^{+0.16}_{-0.16}$	$56.4^{+5.2}_{-3.7}$	990^{+320}_{-380}	$0.20^{+0.05}_{-0.07}$	340
GW170814	$30.7^{+5.7}_{-3.0}$	$25.3^{+2.9}_{-4.1}$	$24.2^{+1.4}_{-1.1}$	$0.07^{+0.12}_{-0.11}$	$53.4^{+3.2}_{-2.4}$	580^{+160}_{-210}	$0.12^{+0.03}_{-0.04}$	87
GW170817	$1.46^{+0.12}_{-0.10}$	$1.27^{+0.09}_{-0.09}$	$1.186^{+0.001}_{-0.001}$	$0.00^{+0.02}_{-0.01}$	≤ 2.8	40^{+10}_{-10}	$0.01^{+0.00}_{-0.00}$	16
GW170818	$35.5^{+7.5}_{-4.7}$	$26.8^{+4.3}_{-5.2}$	$26.7^{+2.1}_{-1.7}$	$-0.09^{+0.18}_{-0.21}$	$59.8^{+4.8}_{-3.8}$	1020^{+430}_{-360}	$0.20^{+0.07}_{-0.07}$	39
GW170823	$39.6^{+10.0}_{-6.6}$	$29.4^{+6.3}_{-7.1}$	$29.3^{+4.1}_{-3.2}$	$0.08^{+0.20}_{-0.22}$	$65.6^{+9.4}_{-6.6}$	1850^{+840}_{-840}	$0.34^{+0.13}_{-0.14}$	1651

Table 1.1: The eleven confident detections provided by The LIGO Scientific Collaboration et al. (2018). Relevant parameters and median values with 90% credible intervals are reported. For binary black hole (BBH) events the redshift was calculated from the luminosity distance and assumed cosmology as discussed in Appendix A. The columns show source frame component masses m_i, chirp mass M_{chirp}, dimensionless effective aligned spin χ_{eff}, final source frame mass M_{fin}, luminosity distance d_L, redshift z and sky localisation $\Delta\Omega$. The sky localisation is the area of the 90% credible region.

2012; De Cia et al., 2018) reproduce a data-driven cosmological evolution.

The distribution of binary coalescences as a function of redshift has been investigated by several authors. In particular, I refer to Dominik et al. (2013). They expressed the metallicity evolution with redshift using a mass-metallicity relation, where the distribution of galaxy masses was given by a Schechter-type probability density function. This last choice is redshift-limited to $z \sim 4$, while metallicity evolution model based on damped Ly-α systems (DLAs) can reach up to redshift $z \sim 5$ (Rafelski et al. (2012), hereafter R2012). Baibhav et al. (2019) investigated the MRD across cosmic time using this approach. I extended my results considering another metallicity evolution model (De Cia et al. (2018), hereafter D2018) which is consistent with the measured solar metallicity in the local universe (Gallazzi et al., 2007). I will provide details on data-driven cosmological evolution in chapter 4.

I will describe in details the data-driven model I developed, in chapter 5.

In chapter 6, I will present the cosmic MRD obtained with my model, for the three DCO classes: DNSs, BHNS, BBHs. I will verify whether these results are consistent with the merging rate confidence intervals provided by LIGO-Virgo (The LIGO Scientific Collaboration et al., 2018). Indeed, LVC inferred merging rates in the local universe from GW detections. I will also compare my results with two previous works, in section 6.4. Neijssel et al. (2019) evaluated the cosmic MRD by means of a similar data-driven approach. An assumed redshift-independent metallicity spread is what mainly differentiates their work with respect to mine. The other comparison was made with Mapelli and Giacobbo (2018), where the authors computed the cosmic MRD by means a full numerical model, that is the cosmological evolution was simulated by Illustris (Vogelsberger et al., 2014).

Chapter 2

Aims

The MRD as a function of cosmological redshift is an essential quantity in GW astronomy. In these years, it is gaining increasing importance because the LVC has planned to improve the sensitivity of GW observatories and enlarge the observatory network.

Among other improvements, I would like to report two facilities which pertain the next future. The European gravitational observatory (EGO) is planning to build the Einstein Telescope (ET), while the US contribution is represented by the Cosmic Explorer (CE). These two new ground-based observatories belong to third generation (3G) observatory network (Reitze et al., 2019). The main characteristic of these new GW interferometers is their capability to observe a merging BBH up to redshift $z \sim 10$. This means that these new instruments can provide data from the early Universe, since the first stars are known to form at redshift $z \sim 7$ (Sobral et al., 2015). Hence, the whole evolutionary life of stellar-born DCOs can be measured. The Einstein Telescope and the Cosmic Explorer will start operating from 2030. A physical quantity that will be fully provided by measures will be the MRD across cosmic time. Until that date, theoretical astrophysicist efforts must aim to assess the predictive power of their models.

In order to evaluate the MRD across cosmic time, the population-synthesis simulations must be put in a cosmological context. In other words, I must convolve the results of population-synthesis simulations as delay time distributions, with star formation rate (SFR) and metallicity evolution model. The *delay time* is the amount of time elapsed from the formation of a compact binary until its coalescence. The delay time distribution depends on physical processes that determine the binary evolution. In chapter 6, I will show how common envelope (CE) ejection efficiency and the natal kick velocity distribution change the value of the MRD. It is now evident how the MRD across cosmic time is essential to track the formation and evolution of a compact binary.

It is possible to evaluate the MRD in two ways. The first case relies on cosmological simulation (Mapelli et al., 2017; Mapelli and Giacobbo, 2018); the second case, the one I present in this Thesis, is based on data-driven models. Cosmological simulations are computationally expensive and thus slow, while a data-driven model

represents a fast framework in which population-synthesis results can be immediately tested. Cosmological simulations, since are run from high redshift ($z \sim 200$) to nowadays, provide metallicity distribution and star formation rate more accurate when considered in the past ($z > 3$). In contrast, empirical cosmological evolution is better constrained at low redshift where the measured quantities are available. In section 6.4, I will compare the results obtained with my semi-empirical model with those generated by a full numerical approach.

Chapter 3

Astrophysics of compact objects

This Thesis can be regarded, from the point of view of the methodology, as a natural prosecution of Giacobbo and Mapelli (2018). In this paper, the authors evaluated the MRD in the local universe ($z = 0.1$) and compared it with the confident interval provided by LVC. In order to obtain the MRD across the entire history of the Universe, I appropriately modified the equation that combines merging DCO catalogues with cosmological evolution. These modifications are shown in chapter 5.

The above-mentioned paper and this thesis share the population-synthesis simulation. In this chapter, I describe the underlying physics that drives a binary system merger; starting from single massive star evolution and supernova (SN) engines, to SN kicks and binary evolution. This chapter wants to provide an outline of the astrophysics of double compact objects.

3.1 Single massive stellar evolution and SNe

Hot massive stars are characterised by strong stellar winds. MOBSE adopted a description of the mass loss ($\dot{M} = \frac{dM}{dt}$) as

$$\dot{M} \propto Z^{\beta}$$

where Z is stellar metallicity and β varies depending on the Eddington factor (Γ_e), as follows

$$\begin{cases} \beta = 0.85, & \text{if } \Gamma_e < 2/3 \\ \beta = 2.45 - 2.4 \cdot \Gamma_e & \text{if } 2/3 \leq \Gamma_e < 1 \\ \beta = 0.05 & \text{if } \Gamma_e \geq 1 \end{cases}$$

This reflects that mass loss becomes almost insensitive to metallicity, in case a massive star approaches or exceeds its Eddington limit, which corresponds the star to be radiation pressure dominated. Figure 3.1 shows the relation between the maximum mass of the compact remnant and the metallicity.

The merging DCO mass distribution reveals two mass gaps. This peculiar mass distribution was first suggested by X-ray binaries and GW are consistent with it

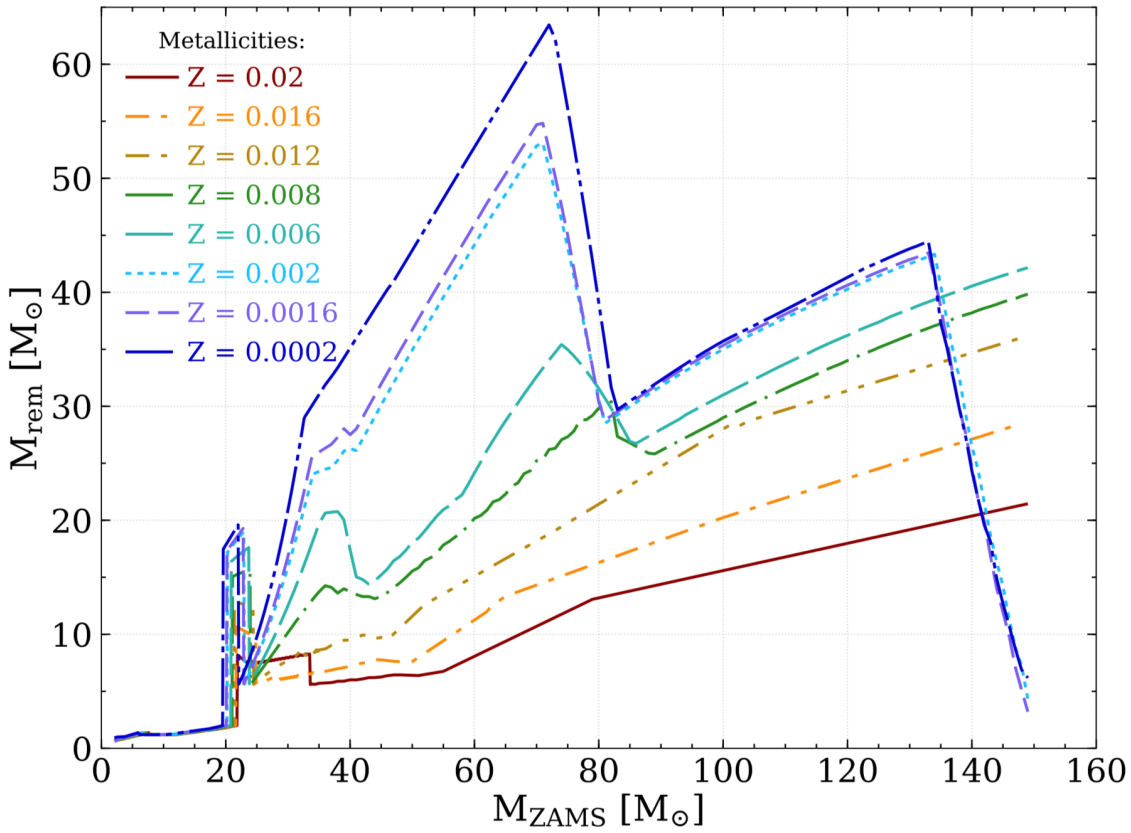

Figure 3.1: Mass of the compact object (M_{rem}) as a function of the mass of the progenitor star (M_{ZAMS}) for 8 metallicities between Z = 0.02 and 0.0002. See Giacobbo et al. (2018a) for details. The curves have been obtained using MOBSE. The rapid SN explosion model is included, as well as the PISNe prescription. Indeed, remnant masses do not exceed the mass gap lower limit ($\sim 60\ M_\odot$)

(Littenberg et al., 2015). The upper mass gap is between 60 $M_\odot$ and 120 $M_\odot$, and it is a consequence of pair-instability supernovae (PISNe) (Spera and Mapelli, 2017). Figure 3.1 shows that no stars leave remnants with $M_{rem} > 60\ M_\odot$, which corresponds to the mass gap lower limit.

The lower mass gap, between neutron star ($M_{NS} < 2\ M_\odot$) and black holes ($M_{BH} > 5\ M_\odot$), can be be reproduced by adopting the prescription of the rapid core-collapse supernovae (CCSNe) mechanism (Belczynski et al., 2012). Giacobbo and Mapelli (2018) considers only the rapid SN model for each simulation, as shown in table 3.1.

Neutron stars (NSs) are also expected to form from via electron-capture supernovae (ECSNe). Indeed, if a growing degenerate oxygeon-neon (ONe) core reaches the mass of

$$M_{ECSN} = 1.38 M_\odot$$

it collapses due to electron-capture on ^{24}Mg and on ^{20}Ne into a neutron star (NS). If the mass core does not exceed the above-mentioned value, a ONe white dwarf (WD) is formed; although it can still collapse to a NS in case it accretes sufficient mass from its companion.

3.2 SN kicks

When a star explodes as a SN and then leaves a remnant, the latter receives a velocity kicks. Any asymmetries in the explosion mechanism can generate this kick. Evidences for such phenomenon come from observations of radio pulsars with excessive velocity with respect to field stars (Hobbs et al., 2005). The velocity distribution is better represented by a Maxwellian function, defined as follows

$$f(v,\sigma) = \sqrt{\frac{2}{\pi}}\frac{v^2}{\sigma^3}\exp\left[-\frac{v^2}{2\sigma^2}\right] \tag{3.1}$$

where $v \in [0,\infty)$. Natal kicks are one of the most debated issues about compact objects, since they have crucial effect on the evolution of DCO. The kicks can either disrupt the binary system or change its orbital properties. A parameter that is affected by these kicks is the eccentricity. In section 3.4, I explain the impact of an enhanced eccentricity on merging efficiency.

Natal kick average velocities are believed to depend on SN mechanisms. Indeed, ECSNe is a rapid process with respect to CCSNe, and thus the asymmetries that generate the natal kick have less time to develop the kick. The consequence is that ECSNe-born NSs are expected to have low natal kicks. Therefore, when an ECSNe occurs, MOBSE draws the SN kick velocity from a Maxwellian distribution (see equation 3.1) defined by a root-mean square equal to

$$\sigma_{ECSN} = 15\,\mathrm{km\,s^{-1}}$$

corresponding to an average velocity $\langle v\rangle_{ECSN} \sim 23$ km s^{-1}. In contrast, NSs born from CCSNe are believed to receive higher kicks. Hence, MOBSE randomly draws the kicks from a Maxwellian velocity distribution characterised, in this case, by a root-mean square equal to

$$\sigma_{CCSN} = 265\,\mathrm{kms^{-1}}$$

which corresponds to an average velocity $\langle v\rangle_{CCSN} \sim 420$ km s^{-1}. However, several studies claim that this velocity distribution underestimates the number of NSs that receive low natal kicks despite the CCSNe mechanism that generates them. For instance, ultra stripped SNe eject a little amount of mass ($< 0.1 M_\odot$) and thus the kick is also small ($< 50\,\mathrm{km\,s^{-1}}$).

Given these uncertainties, Giacobbo and Mapelli (2018) decided to simulate two extreme cases for CCSNe kicks. The *high-velocity* kicks are drawn from a Maxwellian distribution defined by $\sigma_{CCSN} = 265\,\mathrm{kms^{-1}}$; and the *low-velocity* kicks are defined by the Maxwellian distribution that has the same root-mean square of ECSNe kicks. Table 3.1 lists the abbreviations assumed henceforth for the various parameter choices.

Natal kicks have higher impact on NS mergers, because they receive the full kick. In contrast, BHs receive a kick velocity (v_{BH}) that is reduced by the amount of the fallback as

$$v_{BH} = (1 - f_{fb})v$$

where v is the velocity randomly sampled from the Maxwellian distributions and f_{fb} is the fallback parameter. In other words, f_{fb} is the fraction (from 0 to 1) of the

Abbreviation	α	σ_{ECSN} km/s	σ_{CCSN} km/s	SN
$\alpha 1$	1.0	15.0	265.0	Rapid
$\alpha 3$	3.0	15.0	265.0	Rapid
$\alpha 5$	5.0	15.0	265.0	Rapid
CC15$\alpha 1$	1.0	15.0	15.0	Rapid
CC15$\alpha 3$	3.0	15.0	15.0	Rapid
CC15$\alpha 5$	5.0	15.0	15.0	Rapid

Table 3.1: Different parameter prescriptions of the adopted MOBSE simulations (Giacobbo and Mapelli, 2018). The aim was to test the effect of different natal kick velocity distributions and CE ejection efficiencies on compact binaries evolution.

stellar envelope that falls back to the remnant. For the most massive BHs, which are formed silently, without a SN explosion and hence via direct collapse, the fallback parameter is equal to $f_{fb} = 1$ (Fryer et al., 2012).

3.3 Initial conditions

A binary system is defined by the masses and metallicity of the two stars, the period (or semi-major axis) and the eccentricity of the orbit. The mass of the primary star (m_1) is randomly drawn in MOBSE from the Kroupa initial mass functions (Kroupa, 2001), that is

$$\mathcal{F}(m_1) \propto m_1^{2/3}$$

The allowed mass range is $[5M_\odot - 150M_\odot]$. For this set of simulations, it was convenient that MOBSE simulated only massive star. The upper mass cutoff is determined by technical issues. Other population-synthesis code can overcome this limit; for example SEVN (Spera et al., 2015). The mass ratio between the secondary and the primary member of the binary ($q = \frac{m_1}{m_2}$) follows the distribution found by Sana et al. (2012) and it is equal to

$$\mathcal{F}(q) \propto q^{-0.1}$$

with $q \in [0.1 - 1]$. The orbital period P and the eccentricity e distributions are also extracted according to Sana et al. (2012), they are equal to

$$\mathcal{F}(\mathcal{P}) \propto \mathcal{P}^{-0.55}$$

where $\mathcal{P} = \log_{10}(\frac{P}{day}) \in [0.15 - 5.5]$; and

$$\mathcal{F}(e) \propto e^{-0.42}$$

with $e \in [0, 1]$.

For each set of simulations, Giacobbo and Mapelli (2018) considered 12 sub-sets with different metallicities, see table 3.2. The logarithm elements of this array are evenly spaced.

Z	0.0002	0.0004	0.0008	0.0012	0.0016	0.002	0.004	0.006	0.008	0.012	0.016	0.02

Table 3.2: Each binary system is considered to evolve with the same initial metal content. These are the 12 metallicity values with which the adopted MOBSE simulation was run

3.4 Binary evolution

MOBSE adopts a description of binary evolution similar to Hurley et al. (2002). The evolution of two stars in a binary system is characterised by particular features. The physical processes that mainly affect the binary evolution are the mass transfers, the CE phase and the GW emission.

In a binary system, a star can accrete material from the companion in case the latter manifests mass loss due to stellar wind. The average accretion rate on the secondary star, can be estimated according to Hurley et al. (2002) as

$$\langle \dot{m}_{2A} \rangle = -\frac{1}{\sqrt{1-e^2}} \left(\frac{Gm_2}{v_w^2} \right) \frac{\alpha_w}{2a^2} \frac{1}{(1+v^2)^{\frac{3}{2}}} \dot{m}_{1W}$$

where $\langle \dot{m}_{2A} \rangle$ is mass accretion rate on the secondary star, e the eccentricity, v_w is the wind velocity, α_W is an efficiency constant, a the semi-major axis, $\dot{m}_{1W}$ is the mass loss rate from the primary star and v^2 is equal to

$$v^2 = \frac{v_{orb}^2}{v_W^2}$$

where v_{orb} is the orbital velocity. Since $\dot{m}_{1W}$ is quite low ($< 10^{-3} M_\odot yr^{-1}$) and v_w is usually high ($> 1000\,\mathrm{kms}^{-1}$) with respect to the orbital velocity, this kind of mass transfer is usually rather inefficient (Mapelli, 2018). It is although essential to correctly predict the orbital evolution of the binary. Indeed, most of the mass lost by a companion usually does not accrete onto the other, and that translates in an angular momentum loss, which implies circularisation of the orbit.

In contrast, Roche lobe overflow (RLOF) is a mass transfer mechanism that can considerably affect the binary evolution. The Roche lobe is the equipotential surface that surrounds a star which belongs to a binary system. Eggleton (1983) provided the following approximation for the Roche Lobe of the primary star

$$r_{L,1} = a \frac{0.49 q^{2/3}}{0.6 q^{2/3} + \log(1 + q^{1/3})}$$

where q is the mass ratio ($q = m_1/m_2$). The Roche lobe for the secondary star can be obtained by inverting the indices. The two lobes are connected by the L1 Lagrangian point. Since the Roche lobes are equipotential surfaces, matter orbiting at or beyond the Roche lobes can flow freely from one star to the other. Mass transfer obviously changes the mass of the two stars in a binary, and thus the final mass of the compact remnant of such stars, but also the orbital properties of the binary is affected. Mass transfer is usually non conservative and this leads to angular momentum loss, which in turn reduces the orbital eccentricity.

Figure 3.2 shows three different configurations that consider an increasing gradual filling of the Roche lobes (Schmidt, 2016). Figure 3.2(a) shows a detached binary, i.e. each star of the binary system evolves independently unless wind mass transfer sets in. When the most massive star, the primary star, overfills its own Roche lobe, a stable mass transfer to secondary star takes place. This configuration is called semi-detached and it is represented by figure 3.2(b). When an unstable mass transfer sets in or both stars overfill their Roche lobe, a contact binary is formed, as is shown in figure 3.2(c). The subsequent evolution of this type of binary is driven by CE phase (Ivanova et al., 2013). However, if the donor that enters the CE phase is a main sequence star or a Hertzsprung-gap (HG) star, the binary system is forced to merge in MOBSE. Indeed, these type of stars has not yet developed a steep density gradient between the core and the envelope.

The CE phase is described by the $\alpha\lambda$ formalism, which is the most common formalism adopted to model CE. The basic idea is that the energy needed to eject the envelope comes uniquely from the loss of orbital energy of the two cores during the spiral in due to frictional forces, that is

$$\alpha \Delta E_{orb} = \frac{E_{bind}}{\lambda} \tag{3.2}$$

where α quantifies the available energy to unbind the envelope, while λ measures the mass distribution of the envelope. The former is a free parameter, while the letter depends on stellar type (i.e. mass and luminosity), also to account for the contribution of recombinations (Claeys et al., 2014), which are another energy source to unbind the envelope. Therefore, the fate of a binary that entered the CE phase is determined by the following equation

$$\alpha \left(\frac{G m_1 m_2}{2 a_i} + \frac{G m_{1,c} m_{2,c}}{2 a_f} \right) = \frac{G}{\lambda} \left[\frac{m_1 m_{1,env}}{R_1} + \frac{m_2 m_{2,env}}{R_2} \right] \tag{3.3}$$

where a_i and a_f are the initial and final binary separation, m_1 and m_2 are the initial masses of the primary and secondary star respectively, $m_{1,c}$ ($m_{2,c}$) is the primary (secondary) star remnant mass that lost its envelope with mass equal to $m_{1,env}$ ($m_{2,env}$). R_1 and R_2 are the primary and secondary star radius, respectively.

Higher is the α parameter, more efficient is the energy transfer to the envelope, that is the binding energy loss mechanism is more efficient. This implies a less inspiral of the binaries when $\alpha > 1$, that is the probability that the binary survives the CE phase is higher. In order to test the effect of CE on the merging efficiency of DCOs, the adopted population-synthesis simulations assume three different values of CE efficiency, namely $\alpha = 1, 3$ and 5.

Table 3.1 recapitulates the different simulations considered in this Thesis, with the abbreviation used in following legends.

For a binary system to coalesce, its total energy must be equal to zero. Energy is lost by means of CE phase and GW emission. The common envelope rotates more slowly than the orbit of the two cores, so that friction causes them to spiral in and transfer energy to the envelope. This process might release sufficient energy to eject the entire envelope, leaving a close binary containing two naked stellar cores, or it may lead to a premature coalescence of the binary system.

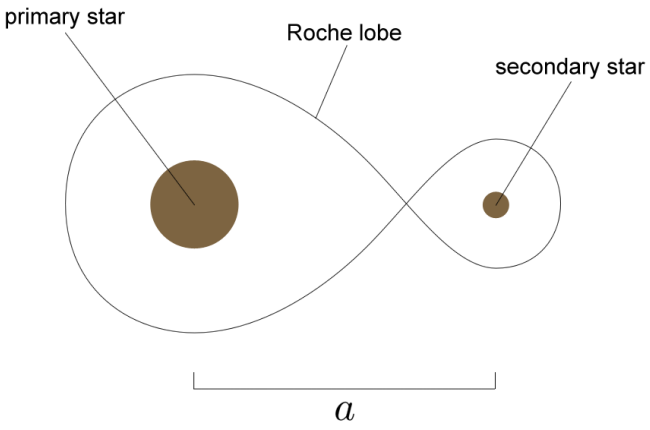

(a) Detached binaries

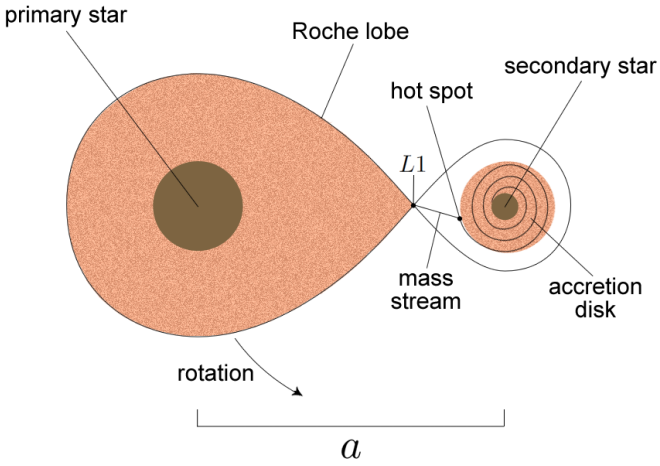

(b) Semi-detached binaries

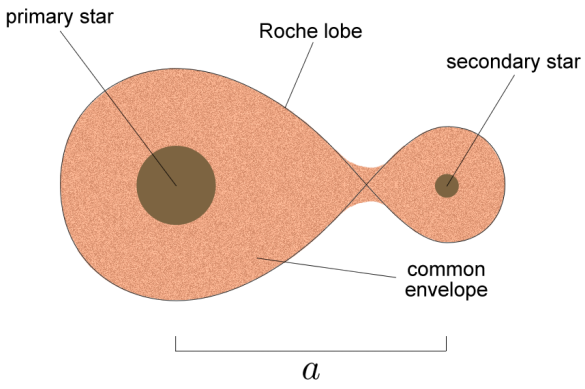

(c) Contact binaries

Figure 3.2: Three different configurations of binary system status with respect to Roche lobe filling. A binary system is detached (3.2(a)) when both companions do not fill their Roche lobes. A semi-detached binary (3.2(b)) is a status characterised by only one star filling its Roche Lobe. When both Roche lobes are overfilled, a contact binary is formed (3.2(c)). Courtesy of Schmidt (2016).

Peters (1964) showed that a binary system is induced to merge because of energy loss from GW emission. The following equation expresses the semi-major axis (a) diminution as a function of binary system parameters, due to GW emission:

$$\frac{da}{dt} = -\frac{64}{5}\frac{G^3 m_1 m_2 (m_1 + m_2)}{c^5 (1 - e^2)^{\frac{7}{2}}} a^{-3} \tag{3.4}$$

where c is the light speed and e is the eccentricity. Equation 3.4 implies that more eccentric binaries have shorter merging times. Thus, moderate natal kicks do not unbind the binary, but increase its eccentricity, shortening its merging time. Since most binaries evolve through processes which tend to circularise their orbits (e.g mass transfer and CE phase), the natal kicks are a fundamental ingredient to obtain highly eccentric orbits. Equation 3.4 depends also on the remnant masses. In chapter 6, I will describe the consequences of binary evolution on the properties of merging DCOs, with particular attention to CE phase efficiency, natal kick velocity distribution and remnant mass spectrum.

Chapter 4

Data-driven cosmological evolution

A satisfactory and complete evolution model of the Universe requires several physical concepts as well as high performance computer facilities. Numerical cosmological simulations are known to be one of the most difficult challenges that astrophysicists have to face. Hydrodynamics is the most representative of these challenges.

In order to put population-synthesis simulations in a cosmological context as quickly as possible, the cosmological evolution can be simplified. Indeed the latter can be represented only by the SFRD and a metallicity evolution model. Since DCOs are stellar born, their number is expected to depend on star formation rate. Similarly, I illustrated in the previous chapter how metallicity can affect the remnant mass and, thus, DCO merger efficiency.

Therefore, I selected the two main contributors to DCO cosmic evolution. In order to better constrain the cosmic evolution, I chose analytic functions directly inferred by data. In this chapter, I will schematically describe these functions, which are the Madau and Dickinson (2014) star formation rate density which represents the state-of-the-art of the subject; and two metallicity evolution models, namely Rafelski et al. (2012) and De Cia et al. (2018).

4.1 Cosmic star formation density

Conceptually, measuring the star formation rate means inferring mass content from integrated light from galaxies. In order to achieve this, Madau and Dickinson (2014) decided to define a conversion factor $\mathcal{K}_\nu$ that relates the specific luminosity L_ν to the SFR. These quantities are operationally related by a convolution

$$\mathrm{SFR} = \mathcal{K}_\nu \times L_\nu$$

where L_ν is express in units of $[\mathrm{erg\,s^{-1}\,Hz^{-1}}]$ and the SFR in units of $[\mathrm{M_\odot\,year^{-1}}]$. The conversion factor $\mathcal{K}_\nu$ varies with the metal content and the star formation history (SFH) of the galaxy, as well as with the choice of the initial mass function (IMF).

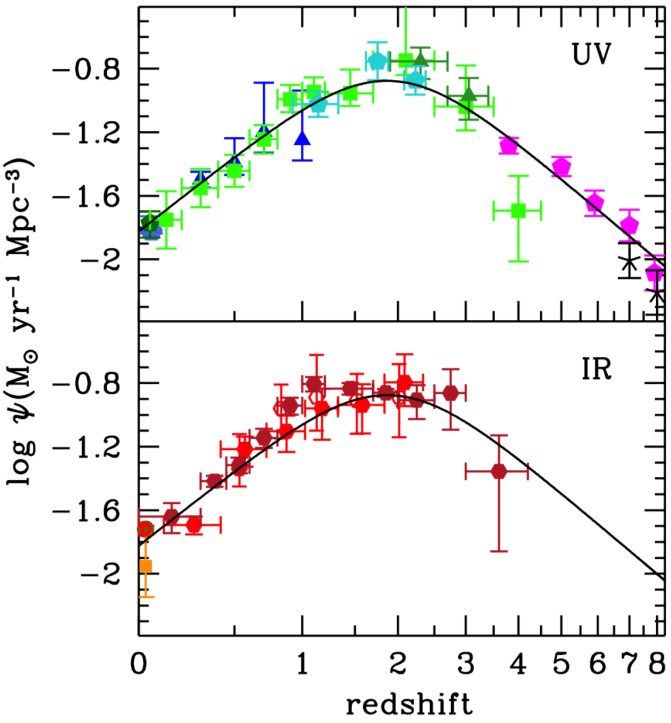

(a) FUV (top) and IR (bottom) data

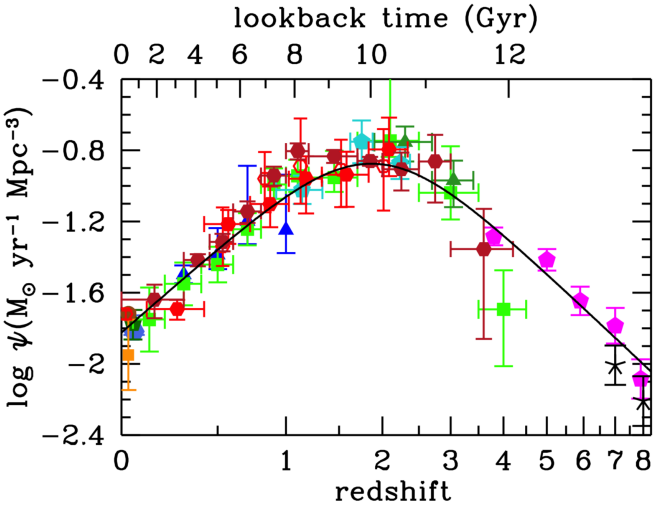

(b) FUV+IR

Figure 4.1: The history of cosmic SFR from Far-UV and IR separately (a) and combined measurements (b). The different sources of data are distinguished by symbols, which are given in table 1 of Madau and Dickinson (2014). The solid curve in the two panels plots is the best-fit of SFRD (see equation 4.1).

The most common tracers of SFR are the UV emissions from massive and young stars and IR radiation. The latter comes from dust emission. These IR photons are those absorbed as UV photons and remitted by dust. Spectra also contains SFR indicators. They are H_α and Lyα. These lines come from recombination due to ionised gas by UV photons.

Madau and Dickinson (2014) considered only surveys that measured SFRs from far-UV (FUV, generally 1500 Å) or mid-IR (MIR) and far-IR (FIR). For their analysis, they stopped at redshift $z \sim 8$. Figure 4.1 shows the cosmic SFRD ($\Psi(z)$) from UV and IR data. The best-fitting function is given by the following equation:

$$\Psi(z) = 0.015 \frac{(1+z)^{2.7}}{1 + \left[\frac{(1+z)}{2.9}\right]^{5.6}} \quad [\mathrm{M}_\odot\,\mathrm{year}^{-1}\,\mathrm{Mpc}^{-3}] \tag{4.1}$$

Coming from the past, a rising phase is noticeable. From redshift $z \sim 8$ to redshift $z \sim 3$, the SFRD scales as $\Psi \propto (1+z)^{-2.9}$. It slows down and peaks at some point between $z = 2$ and 1.5, when the Universe was ~ 3.5 Gyr old. This is followed by a gradual decline to the present day, roughly as $\Psi \propto (1+z)^{2.7}$. The comoving SFR density at redshift $z \sim 7$ was approximately the same as that measured today.

The data-driven cosmological simulation considered in this Thesis adopts Equation 4.1 as expression of the cosmic SFRD.

4.2 Metallicity cosmic evolution models

In this section, I will briefly describe the two adopted metallicity evolution models. These two works required mainly observational efforts. Indeed, they complete the data-driven contributions to my model. I decided to avoid explaining observational details and data reduction procedure, although essential for the results, for the sake of brevity.

4.2.1 Rafelski et al., 2012

The main purpose of Rafelski et al. (2012) is to trace the build-up of heavy elements in neutral gas across cosmic time, by investigating the metal abundances of DLAs, out to $z \sim 5$. This particular class of absorption quasars was chosen because it contains mainly neutral gas. Therefore, DLAs dominate the neutral gas content of the Universe, and exhibit properties indicating that they are neutral-gas reservoirs for star formation at high redshift.

Rafelski et al. (2012) measured the metal abundances of 47 DLAs from $z \sim 0.09$ to $z \sim 5.06$; it is remarkable that 30 of these systems are at redshift $z > 4$. Their data were collected with two instruments on the Keck I and II 10-meter telescope, namely the Echellette Spectrograph and Imager (ESI) and the High Resolution Echelle Spectrometer (HIRES). They also combine their metallicity measurements with 195 DLAs from previous surveys, in order to enlarge the sample.

Figure 4.2 plots the metallicity as a function of redshift for both their measurements and those from literature. In particular, the metallicities from literature are plotted as red crosses, while the green stars are data from ESI and the gold stars from HIRES.

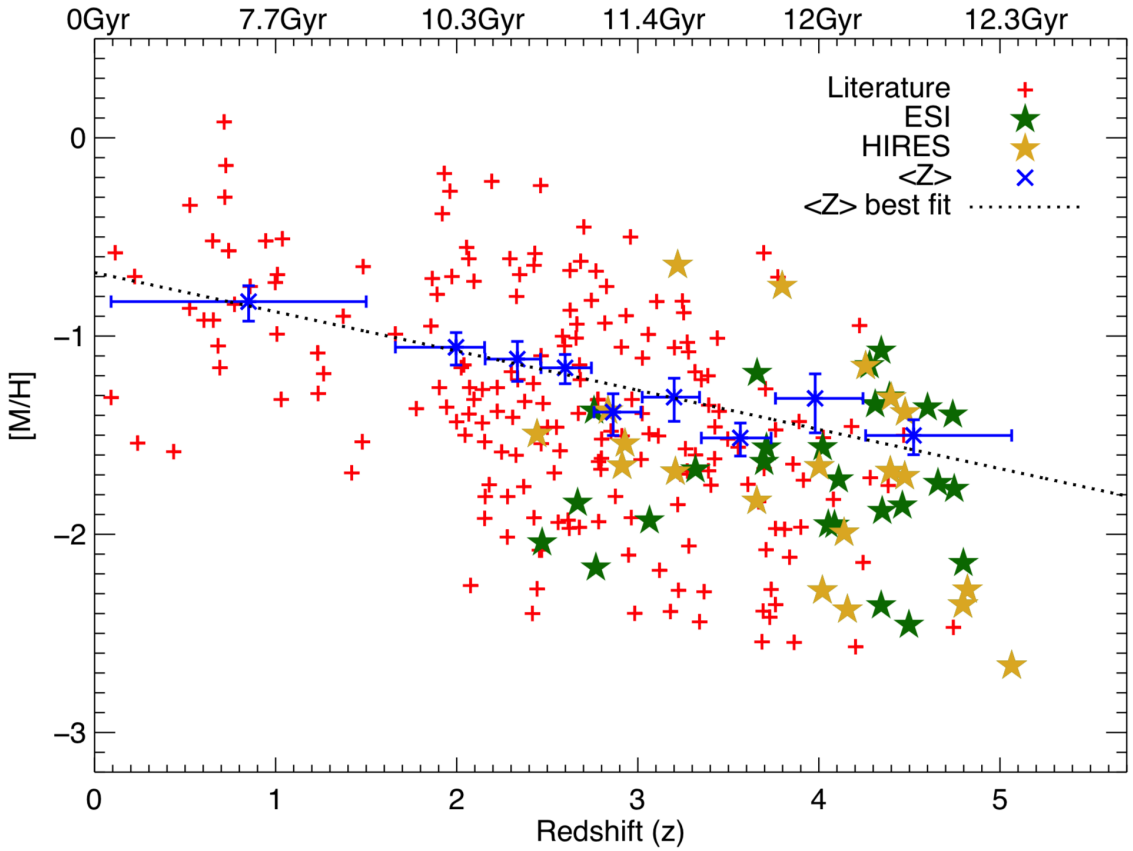

Figure 4.2: Metal abundances [M/H] inferred from damped Ly-α systems as a function of redshift. Red crosses are from literature. The metallicities from ESI are green stars, while those from HIRES are gold stars. The 9 blue crosses with error bars show cosmic average metallicity $\langle Z \rangle$, computed as in equation 4.2. I refer to Rafelski et al. (2012) for further details on error bar determination. The black straight line is the linear fit to the $\langle Z \rangle$ data points, whose expression is equation 4.3.

Among other features, this plot shows an evident dispersion at all redshifts. The dispersion in [M/H] [(1)] is ~ 0.5 dex and does not appear to evolve with redshift. Rafelski et al. (2012) stated that this is not an observational error, but is due to an intrinsic scatter amongst the DLAs. This result was confirmed by successive works, as I will show in the next section (4.2.2).

Another feature of figure 4.2 is that the average [M/H] decreases with increasing redshift. The evolution of [M/H] was investigated by computing the cosmological mean metallicity $\langle Z \rangle$, in the following way

$$\langle Z \rangle = \log \left(\frac{\sum_i 10^{[\mathrm{M/H}]_i} N(\mathrm{HI})_i}{\sum_i N(\mathrm{HI})_i} \right) \tag{4.2}$$

where i represents each bin of DLAs as a function of redshift. Each bin contains an equal number of DLAs, that is 26 DLAs/bin. N_{HI} is the HI column density. Rafelski et al. (2012) confirmed that each DLA has $N_{\mathrm{HI}} > 2 \times 10^{20} \mathrm{cm}^{-2}$ based on the SDSS spectra with spectral resolution FWHM ~ 2 Å.

The black dotted line in figure 4.2 is a linear fit to the $\langle Z \rangle$ values. After performing a χ^2 minimisation, they found that

$$\langle Z \rangle = (-0.22 \pm 0.03) z - (0.65 \pm 0.09) \tag{4.3}$$

This result is in accordance with previous studies, as pointed out by Rafelski et al. (2012).

They performed an analysis that completely neglects dust obscuration. Dust depletion contribution on metal abundances was assessed by De Cia et al. (2018). I present their paper in the next section (4.2.2).

4.2.2 De Cia et al., 2018

De Cia et al. (2018) also provided metal abundances of DLAs from absorption line spectroscopy. They did not neglect the presence of dust, which can affect the metal abundance measurement up to 0.5 dex. The improvement they achieved in this paper was to provide a simplified way, called *single-reference method*, for calculating dust correction.

In a previous paper (De Cia et al., 2016), they found dust-corrected metallicities based on the simultaneous study of the abundances of several metals. This is the most solid method. In contrast, the single-reference method relies only on a single abundance relative to Iron (Fe), that is [X/Fe] . In this case, the dust-corrected metallicity is defined as follows

$$[\mathrm{Fe/H}]_{tot} = [\mathrm{Fe/H}] - \delta_{Fe} \tag{4.4}$$

[(1)] Rafelski et al. (2012) adopted the standard notation where the metal abundance [M/H] signifies the logarithmic abundance of element M relative to solar, namely

$$[\mathrm{M/H}] = \log_{10}(M/H) - \log_{10}(M/H)_{\odot}$$

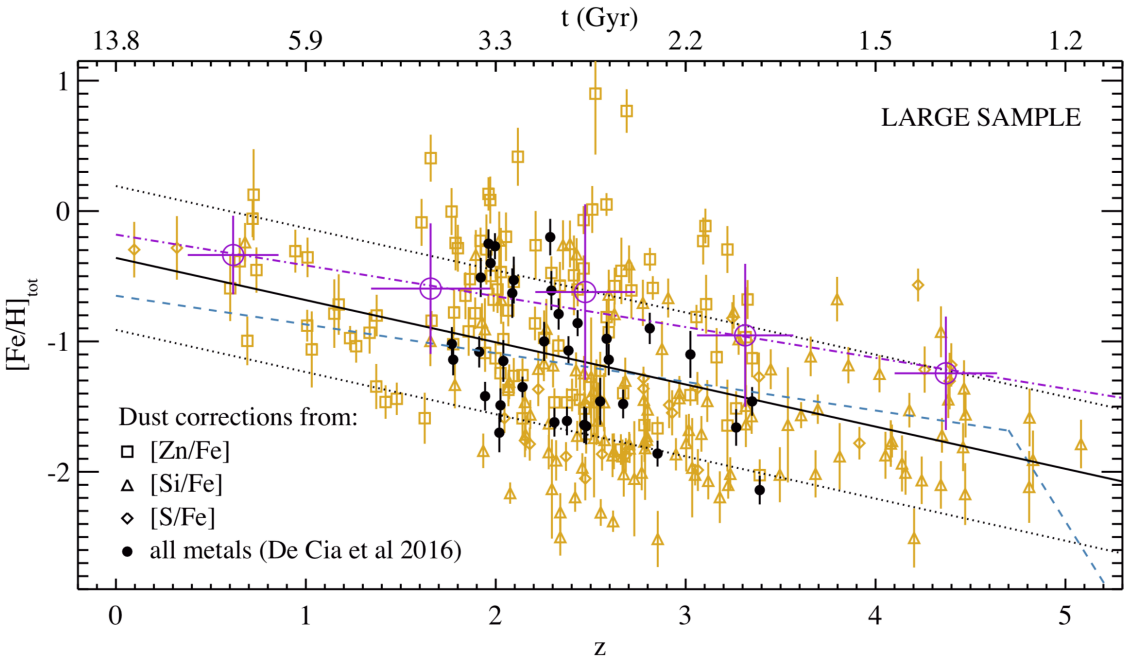

Figure 4.3: Dust-corrected metallicities $[M/H]_{tot}$ derived from several metals simultaneously in De Cia et al. (2016) (black filled circles) and the dust-corrected metallicities $[Fe/H]_{tot}$ calculated with the single-reference method, as shown in equation 4.4, for the large sample (gold open symbols). The shape of the symbols shows which reference was used for dust correction, as labelled in the legend. The black solid and dotted line display the linear fit to the data and the intrinsic scatter of the relation, respectively. The large open purple circles show the mean DLA metallicities weighted for the N(HI) content, in bins of redshift and the linear fit to those points is shown by the dotted-dashed purple line (expressed by equation 4.5). The dashed blue curve shows the average DLA metallicity derived by Rafelski et al. (2012) and the drop at high z is suggested by Rafelski et al. (2014), although it is not considered in this thesis.

where δ_{Fe} is the dust depletion of Fe, computed as

$$\delta_{\mathrm{Fe}} = A2_{\mathrm{Fe}} + B2_{\mathrm{Fe}} \times [\mathrm{X/Fe}]$$

where X is the element on which dust correction is performed, which it can be either Zinc (Zn), Silicon (Si) or Sulphur (S). The coefficients are equal to $A2_{\mathrm{Fe}} = -0.01 \pm 0.03$ and $B2_{\mathrm{Fe}} = -1.26 \pm 0.04$. They applied this single-reference method dust corrections on a large sample, that contains 236 DLAs. The size of this sample is comparable to the one on which Rafelski et al. (2012) performed their analysis.

In Figure 4.3, De Cia et al. (2018) plotted the solid metallicity measurements (black dots) from De Cia et al. (2016), for comparison with the ones obtained with the single-reference method, illustrated in the figure with open gold symbols. They fit a linear regression to these data, although they are not weighted for $N(\mathrm{HI})$ content. They must be weighted to avoid giving too much importance to the low-metallicity systems which carry less gas. Therefore, they computed the weighted neutral gas cosmic average metallicities as in equation 4.3. To this purpose, they divided the sample in bins of redshift ($z < 1$, $1 \leq z \leq 2$, $2 \leq z \leq 3$, $z \geq 4$). The weighted metallicity values are shown in figure 4.3 as purple circles. They performed a linear fit on these data, which yields

$$\langle Z \rangle = (-0.24 \pm 0.14)z + (-0.18 \pm 0.21) \tag{4.5}$$

A consistent comparison can be now done with the metallicity evolution model provided by Rafelski et al. (2012) (see equation 4.2 and dashed blue line in figure 4.3). The two slopes of the metallicity evolution models are very similar, but dust correction provided an intercept 0.4-0.5 dex higher. It approaches solar metallicity ($Z_{\odot} = 0.02$) at redshift zero. This result is rather important, since Gallazzi et al. (2007) estimated from the Sloan Digital Sky Survey (SDSS) that the average metal content (Z_*) in the local Universe ($\langle z \sim 0.1 \rangle$) is consistent with solar metallicity, that is

$$\langle Z_* \rangle = 1.04 \pm 0.14 \ Z_{\odot}$$

where $Z_{\odot}$ is assumed equal to 0.02.

This relation of metallicity with redshift also shows a large scatter (~ 0.5 dex). As I mentioned in the previous section, Rafelski et al. (2014) found a similar result. At any given redshift, we expect that DLAs may select galaxies with a range of different masses and metallicities. The scatter of metallicity versus redshift is therefore physical and it reflects a spread in metallicity. Considering a mass metallicity relation (Tremonti et al., 2004), a galaxy with little mass will contribute less to the average metallicity evolution.

From a cosmological point of view, the metal content evolution with redshift is better approximated by a metallicity distribution defined by a redshift-independent spread and a redshift-dependent metallicity average value. In order to obtain such relation, one possible way to proceed is to convolve a mass-metallicity relation (MZ) with a galaxy-stellar mass function (GSMF) as Neijssel et al. (2019) performed in their paper. In section 6.4, I will compare my results with theirs, in order to assess the effective contribution of a metallicity spread on the MRD across cosmic time.

Chapter 5

The data-driven model

In this chapter, I will describe the procedure to calculate the MRD across cosmic time. Appendix B includes the Python script that implements this methodology.

5.1 Merging efficiency

For each simulation set (see table 3.1), I evaluated the number of merging DCOs per unit mass, also known as *merging efficiency* and denoted as η, in the following way

$$\eta_i = f_{bin} f_{\rm IMF} \frac{N_{merger,i}}{M_{tot,sim}} \quad [\mathrm{M}_\odot^{-1}] \tag{5.1}$$

where i stands for the three different classes of DCOs, which are DNS, BBH, BHNS. $N_{merger,i}$ is the number of DCOs that merge within an Hubble time. The latter is equal to

$$t_{H_0} = \frac{1}{H_0} = 14.4 \pm 0.2 \text{ Gyr}$$

where the Hubble constant $H_0 = 67.8 \pm 0.9 \text{ km s}^{-1} \text{ Mpc}^{-1}$. $M_{tot,sim}$ is the total initial mass of the simulated stellar population. This quantity is different for every simulation set. Indeed, the number of simulated binaries is fixed and corresponds to 1.2×10^8 binary systems, but the total initial mass is randomly drawn from the IMF, as explained in section 3.3. In addition, $f_{\rm IMF} = 0.285$ is a correction factor that takes into account the fact that the MOBSE simulation adopted in this thesis, considered only systems which have primary component more massive than 5 $M_\odot$. Another correction factor is f_{bin} which takes into account the fact that the simulation evolves only binary systems. Assuming that 50 % of the stars are in binary systems, $f_{bin} = 0.5$ (Sana et al., 2012)). Figure 5.1 shows η as a function of the metallicity Z for each simulation set and separately for each class of DCOs (Giacobbo and Mapelli, 2018). The number of mergers per unit mass spans a large range of values depending on natal kicks, on CE efficiency and progenitor metallicity.

η strongly depends on progenitor metallicity for both BBHs and BHNSs. In particular, η_{BBH} is at least $\gtrsim 3$ orders of magnitude higher at low metallicity than

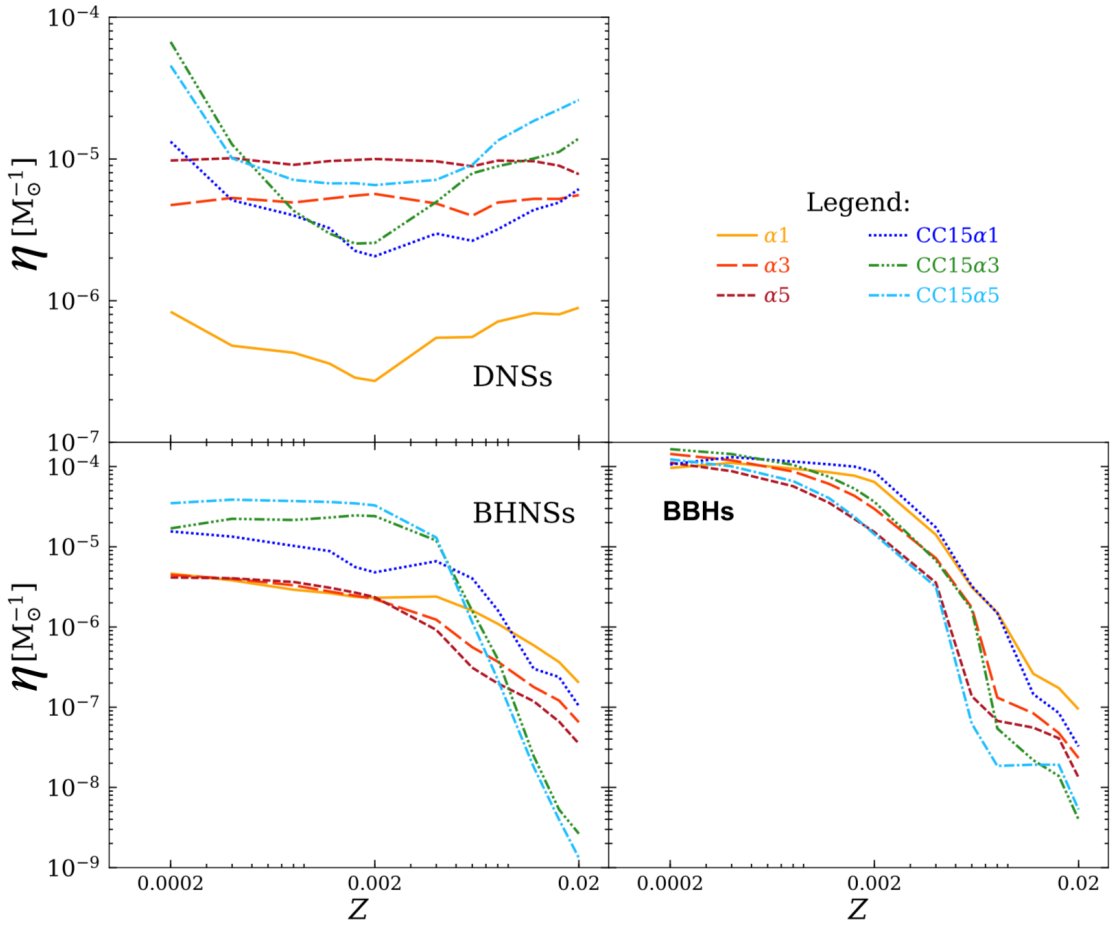

Figure 5.1: Number of merging DCOs per unit mass (η) as a function of progenitors metallicity for all the adopted simulations (see table 3.1). Top-left panel: merging DNSs; bottom-left panel: merging BHNS; bottom-right panel: merging BHBs (Giacobbo and Mapelli, 2018).

at high metallicity. Similarly, $\eta_{BHNS} \gtrsim 2$ orders of magnitude greater at $Z = 0.0002$ rather than at $Z = 0.02$. This is due to the strong dependence of equation 3.4 on remnant masses ($\propto m^3$), which are in turn strongly affected by progenitor metallicity, as shown in figure 3.1. Hence, binary systems born in a metal-poor environments tend to merge more efficiently.

In contrast, the number of DNS mergers per unit mass η_{DNS} does not show almost any dependence on Z, in run $\alpha 3$ and $\alpha 5$. In the other simulations, η_{DNS} is significantly lower for progenitor's metallicity $Z = 0.002$ than for progenitors with higher or lower metallicity. This happens because stellar radii of $\sim 8-20\ M_\odot$ stellar progenitors tend to reach larger values at $Z \sim 0.002$ than at other metallicities, in MOBSE.

5.2 MRD across cosmic time

The delay time, that is the time elapsed between a formation of a binary and its coalescence is defined in MOBSE as follows

$$t_{delay} = t_{evol} + t_{GW} \tag{5.2}$$

where t_{evol} is the time elapsed from the binary system formation as two ZAMS stars, until the collapse of both progenitors. In the isolated evolution environment, if the binary system survives the CE phase, the only mechanism that can disperse total energy is GW emission. This energy loss mechanism is described by equation 3.4. From this equation, it is possible to derive the expression for the time elapsed for disperse the total energy by GW emission, which yields

$$t_{GW} = \frac{5}{256}\frac{c^5}{G^3}\frac{a^4(1-e^2)^{7/2}}{m_1 m_2(m_1+m_2)} \tag{5.3}$$

This amount of time is exceedingly higher than the time the massive binary system takes to evolve. For example, in a typical situation, a BBH with masses $(10-10)\ M_\odot$, with initial major-axis $a = 10\ R_\odot$ and eccentricity $e = 0.5$, takes $t_{GW} \sim 3$ Gyr to merge.

Figure 5.2 shows the delay time distribution ($\mathcal{T}_{delay}$) for each simulation set. The contribution of initial metallicities are summed over in these plots. It is worth noting that number of merging BBHs is always greater than the number of the other merging DCOs. This is due the fact that t_{GW} (see equation 5.3) strongly depends on remnant masses, namely $t_{GW} \propto m^3$. In other words, since BBHs are always more massive than the other DCO types, this translates in an higher merging efficiency. The $\mathcal{T}_{delay}$ trend is slightly affected by the three α parameters and the natal kick velocity distributions. Indeed, in any case it is compatible with $dN/dt \propto t^{-1}$. This function is represented by the dot-dashed black line in figure 5.2. The binary evolution free parameters affect mainly the total number of merging DNSs, as shown previously in figure 5.1. For instance, CC15α5 that is an efficient CE ejection and a low natal kick velocity distribution, provides a DNS delay time distribution that is comparable with the BBH one.

The BBH delay time distribution is mainly affected by the metal content of the progenitor stars. Figure 5.3 shows the delay time distribution obtained with an efficient CE prescription and fast natal kicks (α5, 5.3(a)) and slow natal kicks (CC15α5 ,5.3(b)). Different initial metallicities (table 3.2) are grouped in two sets: low metallicities ($Z < 0.0012$) and high metallicities ($Z > 0.0016$). It is worth noting that the majority of BBHs that are born from metal-poor stars tend to merge with short delay time ($t_d < 1$ Gyr). BBHs that merge with long delay time ($t_d > 1$ Gyr) are born from stars with initial metallicity greater that $Z > 0.0016$. This trend is even more evident for systems with considerably high delay time ($t_{delay} > 6$ Gyr). Indeed, merging system fraction remains constant for metal-poor progenitors, while drops to zero for metal-rich progenitors. Lower SN kick velocities mildly affect the delay time distribution slopes. Indeed, BHs receive natal kicks that are reduced by the fallback parameter, as shown in section 3.2.

In section 4.2, I showed how the average metal content of the Universe decreases at increasing redshift. Therefore, the delay time distribution of DCOs that form at

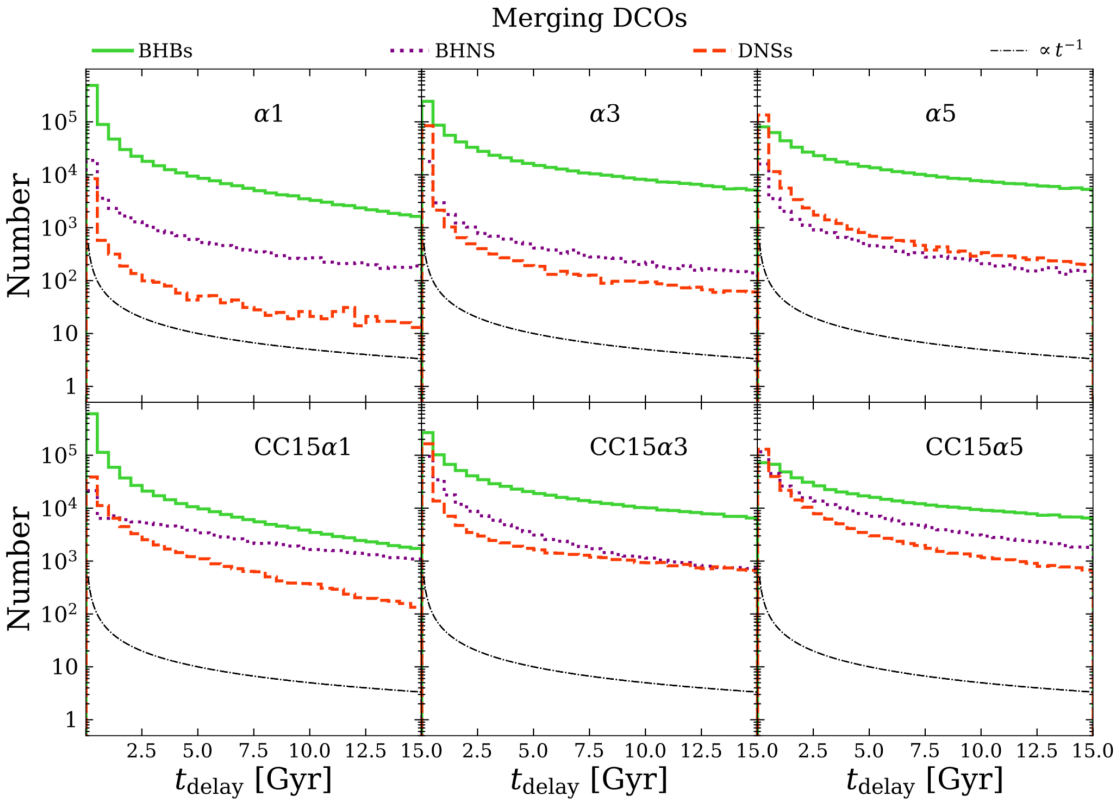

Figure 5.2: Delay time distribution ($\mathcal{T}_{delay}$) for DNSs (dashed red line), BHNSs (dotted violet line), and BHBs (green solid line) for all simulation sets. Giacobbo and Mapelli (2018) summed over different metallicities. Thin dot-dashed black line is $\dot{N} \propto t^{-1}$. The bin width is 0.5 Gyr

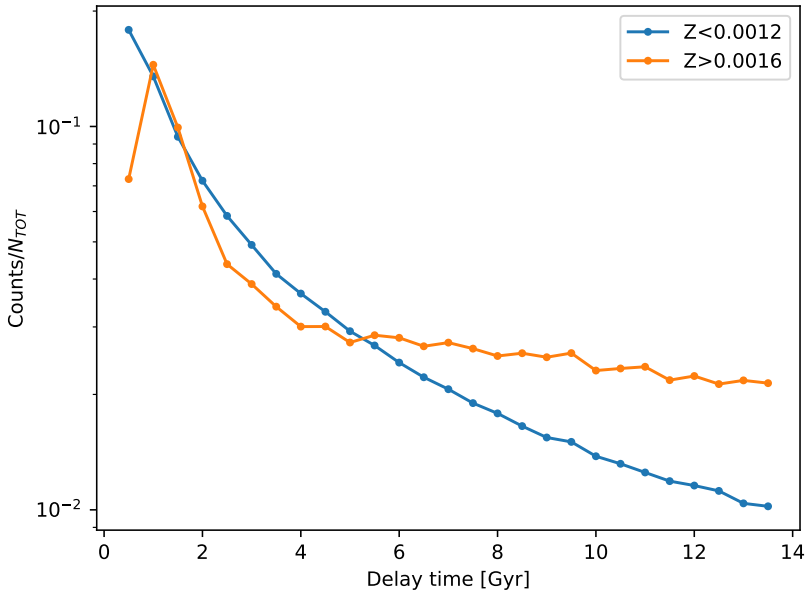

(a) BBHs - $\alpha 5$ - high kicks

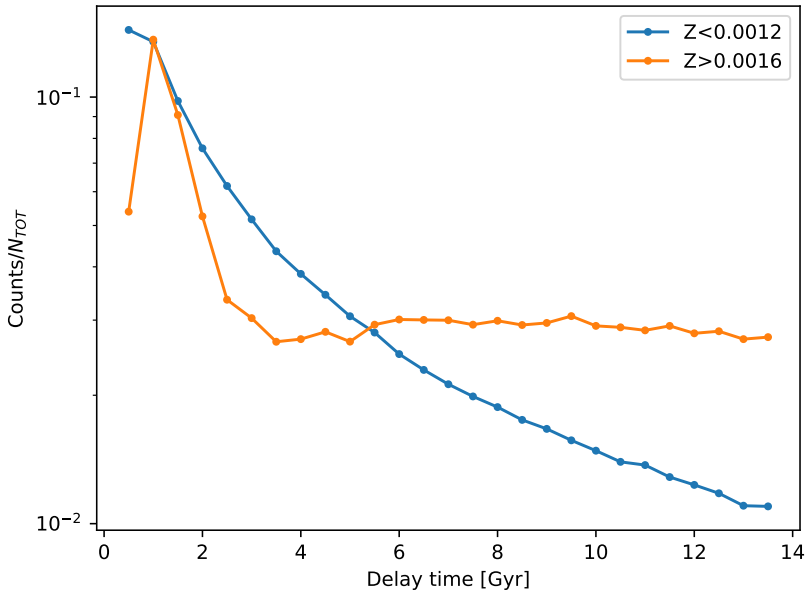

(b) BBHs - CC15$\alpha 5$ - low kicks

Figure 5.3: Delay time distributions for BBHs obtained with an efficient CE ejection prescription and high kicks (a) and low kicks (b). Initial metallicities are grouped in two sets: low metallicities ($Z < 0.0012$) and high metallicities ($Z > 0.0016$). The bin width is 0.5 Gyr. Each histogram is normalised by the total number of counts.

Paper	Abbreviation	Metallicity evolution model
Rafelski et al. (2012)	R2012	$\langle Z \rangle = (-0.22 \pm 0.03)z - (0.65 \pm 0.09)$
De Cia et al. (2018)	D2018	$\langle Z \rangle = (-0.24 \pm 0.14)z - (0.18 \pm 0.21)$

Table 5.1: Metallicity evolution models as a function of redshift considered for the evaluation of the MRD across cosmic time. The first column shows the reference paper, the second the abbreviation adopted in the forthcoming legends, and the third the results of linear fits on observational data. I implemented the conversion $Z = 0.02 \cdot 10^{\langle Z \rangle}$ to match the scale of the initial metallicities reported in table 3.2.

high redshift is associated with initial low metallicity of the progenitors. DCOs that form in different metallicity environments are expected to have different delay time distributions as well as different formation redshifts.

Table 5.1 recapitulates the two metallicity evolution models adopted in the forthcoming analysis. They express the average metal content of the Universe as linear functions of cosmological redshift.

The procedure, I developed to evaluate the cosmic MRD, consists on counting how many DCOs merge at a given redshift z that formed in every higher redshift ($z' > z$). To this purpose, I defined a redshift binning that goes from $z = 15$ to $z = 0$ with a constant step equal to $\Delta z = 0.1$. In order to compute the total mass of stars formed within a specific redshift bin, I considered the SFRD presented in section 4.1. This quantity must be multiplied by η_i in order to obtain the fraction of the total merging mass at a given redshift. I then defined the merger time t_{merger} as

$$t_{merger}(z', z) = t_{form}(z') - t_{delay}(z, Z(z')) \tag{5.4}$$

t_{delay} is the delay time of a single binary generated by the simulation associated with initial metal content Z, which is derived by either Rafelski et al. (2012) or De Cia et al. (2018) metallicity models, computed on z'. Since the initial metallicity set (see table 3.2) is not linearly evenly spaced, I had to choose the delay time distribution associated with the closest metallicity available. This implies a non-smooth MRD evolution as a function of redshift (see chapter 6). t_{form} is the formation time corresponding to the lookback time computed at formation redshift z'. The lookback time is given by the following equation:

$$t_{lb}(z) = \frac{1}{H_0} \int_0^z \frac{dz'}{(1+z')\sqrt{\Omega_m(z+1)^3 + \Omega_k(1+z)^2 + \Omega_\Lambda}} \tag{5.5}$$

where Ω_m, Ω_k and Ω_Λ are the density parameters (see appendix A for the adopted cosmology and Hogg (1999) for reference).

The merger time distribution $\mathcal{T}_{merger}$, computed with the values in equation 5.4, must be divided by $N_{merger,i}$, the total number of merging objects, in order to obtain the fraction of merging DCO at given formation redshift bin. I implemented the concepts developed thus far in the following integral:

$$\mathrm{MRD}_i(z) = \frac{1}{t_{lb}(z)} \int_{z'=15}^{z} \frac{\mathcal{T}_{merger,i}(z', z)}{N_{merger,i}} \, \mathrm{SFRD}(z') \, \eta_i(Z(z')) \, \frac{dt_{lb}}{dz'} dz' \tag{5.6}$$

where $\frac{t_{lb}}{dz'}$ is given by

$$\frac{dt_{lb}}{dz'} = \frac{1}{H_0} \frac{1}{(1+z')\sqrt{\Omega_m(z'+1)^3 + (1-\Omega_m)}} \tag{5.7}$$

and $t_{lb}(z)$ is expressed as in equation 5.5 with $\Omega_k = 0$ since a flat Universe is considered. I must multiply by the lookback time because the relation between redshift and time is not linear.

The next chapter (6) illustrates the results obtained by computing this equation for the three different classes of DCOs and different parameter choices of the population-synthesis simulation, namely α parameter and natal kick velocity distribution. I compared then the results obtained with the two different metallicity evolution models.

Chapter 6

Results

In this chapter, I will present the results obtained evaluating equation 5.6 for each population-synthesis prescription (see table 3.1), for each metallicity evolution model (see table 5.1) and for each class of DCOs, namely DNSs, BHNSs and BBHs. I will also provide a comparison of my results with those obtained by two previous works (see section 6.4).

Each figure presented hereafter includes the LIGO-Virgo confidence intervals, presented in the first gravitational-wave transient catalogue (GWTC-1) of compact binary mergers. The GW events were detected by LVC interferometers, during the first and the second observing run (The LIGO Scientific Collaboration et al., 2018). The merging rates inferred from GW detections at 90% credible intervals are shown in table 6.1. These merger rate intervals are limited to the observing horizon of LIGO and Virgo, which is currently $z \in [0, 1]$. The detectability of a merging binary depends naturally on a series of parameters, for example the merging masses. A BBHs of mass $(10 - 10)M_{\odot}$ can be detected up to redshift $z \sim 0.2$ (Baibhav et al., 2019). Since there are too few GW detections so far in the redshift interval $z \in [0, 1]$, LVC do not consider a MRD evolution with redshift. Therefore, the credible intervals shown in table 6.1 have to be considered redshift-independent.

Every figure presented in the following sections, from 6.1(a) to 6.3(b), has some common features.

DCO class	MRD [$\mathrm{Gpc^{-3}y^{-1}}$]
DNS	[110 - 3840]
BBH	[9.7 - 101]
BHNS	[- 610]

Table 6.1: Merger rates inferred from the LIGO-Virgo detections for the three classes of DCOs, at 90% credible intervals (The LIGO Scientific Collaboration et al., 2018). The DNS LIGO-Virgo credible interval is inferred by the single detection GW170817. This fact explains the large uncertainty span. Since a BHNS merger has not yet been observed in O1 and O2, only an upper limit can be determined.

Each cosmic MRD shows a similar trend, namely it increases at increasing redshift up to a peak and then decreases. If metallicity did not play a role and if delay time was extremely short, we would expect a peak of MRD coincident with the maximum of the SFRD, that is at $z \sim 2$ (see equation 4.1). When $\alpha 5$ CE ejection efficiency is considered, each DCO class shows its MRD that peaks at $z \sim 2$, see figure 6.1 for DNSs, figure 6.2 for BBHs and figure 6.3 for BHNS. This trend is independent on the assumed metallicity evolution model. However, some MRD peaks are anticipated or delayed with respect to the SFRD maximum. This can be explained as follows. First, some merging efficiencies strongly depend on progenitor's metallicity, especially BBHs and BHNSs, but even some models of DNSs show a mild trend with Z, see figure 5.1. Second, the distribution of delay times depends on several population-synthesis features and on metallicity, as I showed in figure 5.2 and 5.3. For instance, CC15α5 in figure 6.1(b) shows a maximum at redshift $z \sim 1$, while CC15α1 peaks at $z \sim 1.4$. In contrast, BBHs tend to merge mainly at redshift $z > 2$. Figure 6.2(a) shows the peaks at redshift $z > 2$ for $\alpha 1$ and $\alpha 3$, independently on the natal kick velocity distributions. This trend is still more evident once De Cia et al. (2018) (hereafter D2018) metallicity evolution model is considered (see figure 6.2(b)). CC15α1 and $\alpha 1$ population-synthesis prescriptions are responsible for MRD peaks close to redshift $z \sim 3$. This is due to the fact that D2018 model selects at the redshift where the SFRD peaks, binary population that have an higher initial metallicity, with respect to Rafelski et al. (2012) metallicity evolution model (hereafter R2012). These binaries eventually merge with long delay times, and this explains why the SFRD peak is lowered with respect to R2012 model. Figure 5.3 shows that the fraction of merging BBHs that have delay times longer than 10 Gyr is still consistent, only if they are born from metal-rich progenitor stars .

Another common feature is the MRD non-smooth trend. A part from the MRD evaluated with $\alpha 5$ prescription for DNS, which is undoubtedly continuous, the other functions are segmented. This is due to the fact that the population-synthesis simulation initial metallicities are not linearly spaced, and thus the metallicity changes abruptly at increasing redshift. This fact clearly is not physical and it can be avoided either running population-synthesis simulations with a lot more initial metallicities, which is computationally expensive, or inserting in the data-driven model a metallicity spread, independent with redshift. This spread indeed takes into account the physical fact that DCOs evolve with different initial metallicities although they form at the same redshift.

In sections 6.1, 6.3 and 6.2, I will focus on the impact of the metallicity evolution models and population-synthesis prescriptions on MRD evolution, for each DCO type.

6.1 DNS MRD Evolution

Figure 6.1 shows the MRD across cosmic time for DNSs, evaluated with Rafelski et al. (2012) (R2012, figure 6.1(a)) and De Cia et al. (2016) (D2018, figure 6.1(b)) metallicity evolution models, for the various binary evolution prescriptions.

In both figure, the cosmic MRD is characterised by large spread due to the different population synthesis prescriptions adopted. This is expected because the merging efficiency (η, see figure 5.1) varies by an order of magnitude between $\alpha 1$

and $\alpha 5$. However, the assumed metallicity evolution model still affects the MRD. Indeed, at redshift $z = 0.1$ with R2012 model, the MRD evaluated with CC15$\alpha 5$ is lower with respect to $\alpha 5$. This at first sight is controversial, because lower natal kicks should increase the merger rate. I can explain this controversy by looking again at figure 5.1. I notice that CC15$\alpha 5$ merging efficiency is lower than $\alpha 5$ until $Z = 0.006$. R2012 metallicity evolution model predicts indeed a lower metal content at redshift zero. This trend is inverted considering D2018 model. Indeed, in figure 6.1(b), CC15$\alpha 5$ is higher than $\alpha 5$ because this metallicity evolution model predicts solar metallicity ($Z = 0.02$) in the local Universe.

Since η computed with $\alpha 5$ is independent on metallicity, consequently the cosmic MRD varies smoothly at increasing redshift, since it is driven by the SFRD evolution only. Indeed, it peaks at redshift $z \sim 2$.

The MRD evaluated with the R2012 model is compatible with the LIGO-Virgo credible interval only considering the most efficient CE ejection simulated, that is $\alpha 5$ and low natal kicks CC15$\alpha 5$. D2018 metallicity model allows also CC15$\alpha 3$ to be consistent with LIGO-Virgo confidence interval. This means that a less efficient CE ejection can reproduce the merging rate density measured in the local universe, once considering a more robust metallicity model. I remind that De Cia model is consistent with the measured solar metallicity in the local universe, see section 4.2.2.

It is worth explaining why CC15$\alpha 3$ (purple line) evidently drops from $\sim 1000\,\mathrm{mergers\,Gpc^{-3}yr^{-1}}$ to $\sim 300\,\mathrm{mergers\,Gpc^{-3}yr^{-1}}$ at redshift $z \sim 5$. This trend is shared by both metallicity evolution models. I can explain this fact, from figure 5.1 where is possible to notice that η evaluated with CC15$\alpha 3$ prescription decreases up to 8×10^{-5} at metallicity $Z = 0.002$.

6.2 BBH MRD Evolution

Figure 6.2(a) and 6.2(b) show a narrow spread in the BBH cosmic MRD considering different population-synthesis prescriptions. This is expected according to η which instead shows evident variations with Z (see figure 5.1). It is therefore essential the impact of metallicity on merging efficiency.

Since there have been ten BBH detections so far, the LIGO-Virgo confidence interval is narrower with respect to those of the DNSs. Reproducing the MRD in the local universe represents still a challenge. R2012 metallicity model (see figure 6.2(a)) at redshift $z = 0.1$ predict one order of magnitude more merger rate density with respect to the LIGO-Virgo confidence interval upper level. This is due to the fact that the metallicity at redshift zero, predicted by R2012 mode, is still too low, namely $Z = 4 \times 10^{-4}$ (see table 5.1).

D2018 model (figure 6.2(b)) predicts the same order of magnitude merger rate density of the LIGO-Virgo credible interval upper level at redshift zero, but still is not consistent.

From figure 6.2(a) it is possible to notice how low kicks are responsible of a mild increase of the MRD. The BH natal kicks are reduced by the fallback amount.

An efficient CE phase ($\alpha 5$) produces an higher MRD than a less efficient one ($\alpha 1$) at redshift $z = 0.1$. Therefore, $\alpha 1$ is the closest to the upper limit of the LIGO-Virgo confidence interval. The impact of CE efficiency on MRD is then reversed

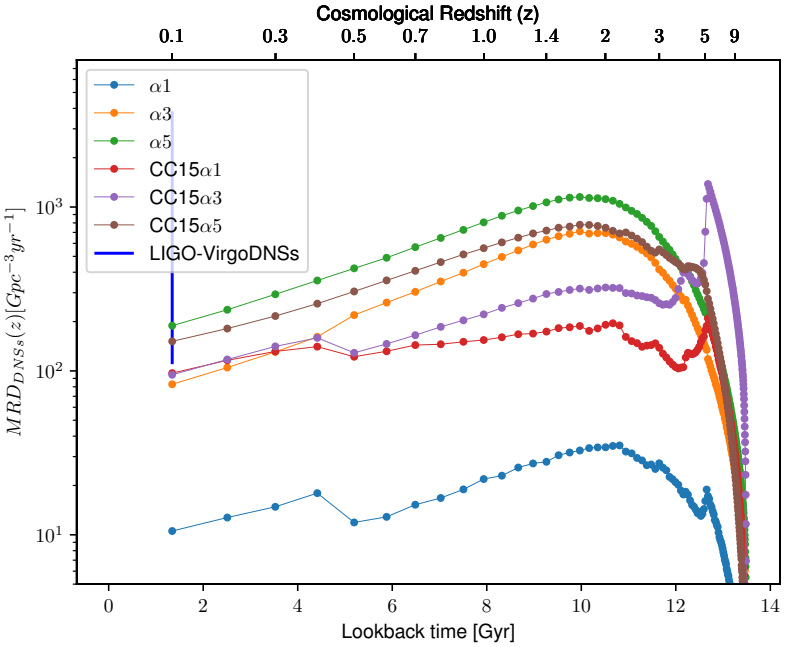

(a) DNSs - Rafelski

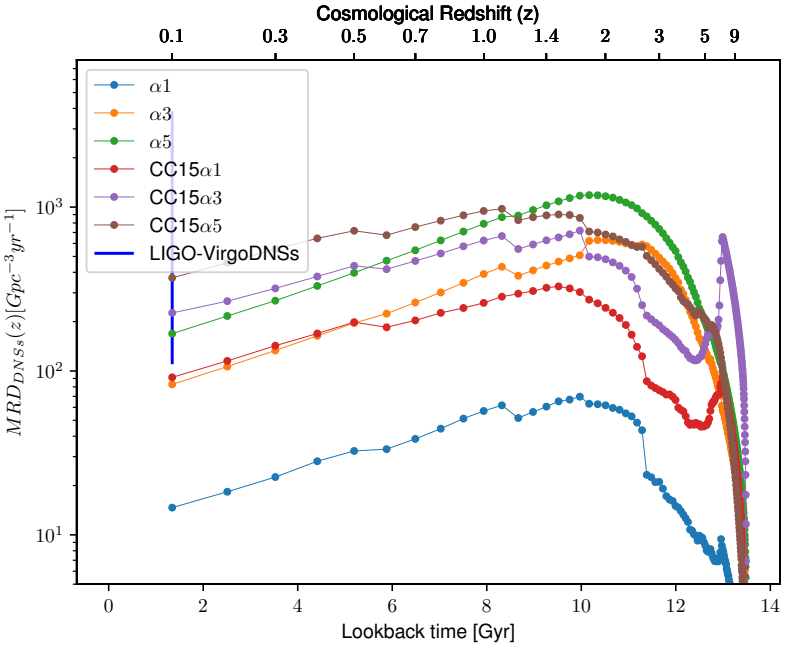

(b) DNSs - De Cia

Figure 6.1: The cosmic DNS MRD evaluated with Rafelski et al. (2012)(a) and De Cia et al. (2016) (b) metallicity evolution model, for the various population-synthesis prescriptions (see table 3.1). The DNS LIGO-Virgo confidence interval (blue vertical line) is shown as a comparison (see table 6.1) and it placed at redshift $z = 0.1$ for simplicity

with respect to DNSs. This might be due to a different CE evolution for DNSs and BBHs. The data available so far cannot constrain this, which might be confirmed once the Einstein Telescope and Cosmic Explore will be operating.

6.3 BHNS MRD Evolution

The BHNS cosmic MRD (see figure 6.3(a) and 6.3(b)) is characterised by a combination of features peculiar of DNSs and BBHs. Indeed, it is still evident a large spread due to different population-synthesis prescriptions; and metallicity evolution strongly affects the MRD. D2018 model predicts an order of magnitude less merging rate density with respect to R2012, at redshift $z = 0.1$. Therefore, every population-synthesis prescription coupled with D2018 is compatible with the upper-level inferred by LIGO-Virgo.

6.4 Comparisons with literature

In this section, I compare the MRD density obtained with $\alpha 5$ CE ejection efficiency prescription and two previous works. The purpose of these works is to predict the MRD as a function of redshift, although with different approaches.

6.4.1 Neijssel et al. (2019)

The first paper (Neijssel et al. (2019), hereafter N2019) relies on merging DCO catalogues obtained with COMPASS, which is another upgrade of the BSE population-synthesis code. In this work they do not explore the impact of various population-synthesis prescriptions on MRD. However, they implemented a metallicity evolution model characterised by a redshift-independent metallicity spread. They compared different metallicity-specific star formation rates (MSSFR) computed with the following expression

$$\frac{d^3 M_{SFR}}{dt_s dV_c dZ} = \frac{d^2 M_{SFR}}{dt_s dV_c} \times \frac{dP}{dZ}(z)$$

where Madau and Dickinson (2014) SFR was adopted, although N2019 left two free parameters to be constrained with gravitational-wave observations. The metallicity density function ($\frac{dP}{dZ}(z)$) was obtained by convolving a series of galaxy stellar mass functions with mass-metallicity relations, in order to take into account of the significant uncertainties whose these functions are affected. In figure 6.4 I reported their results obtained with Barrett et al. (2018) approach only. The MZ relation was given by Langer and Norman (2006) with a redshift-independent GSMF (Panter et al., 2004).

Figure 6.4(a) shows the DNS MRD. This is the case where my results are easily comparable with Neijssel et al. (2019) method. In fact, the cosmological environment only mildly affects the DNS mergers. This was already recognised from figure 6.1(a), where the MRD obtained with R2012 and D2018 metallicity evolution models are also very similar.

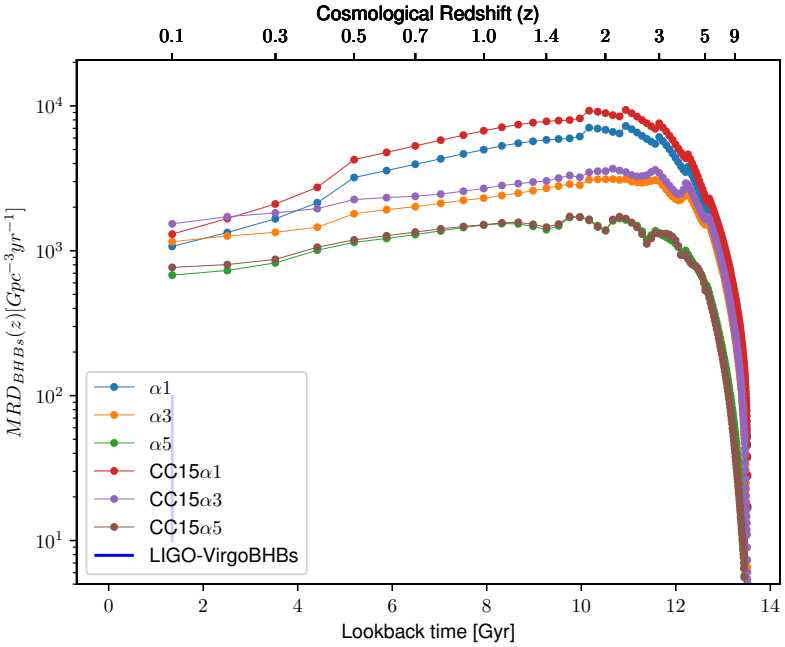

(a) BBHs - Rafelski et al.,2012

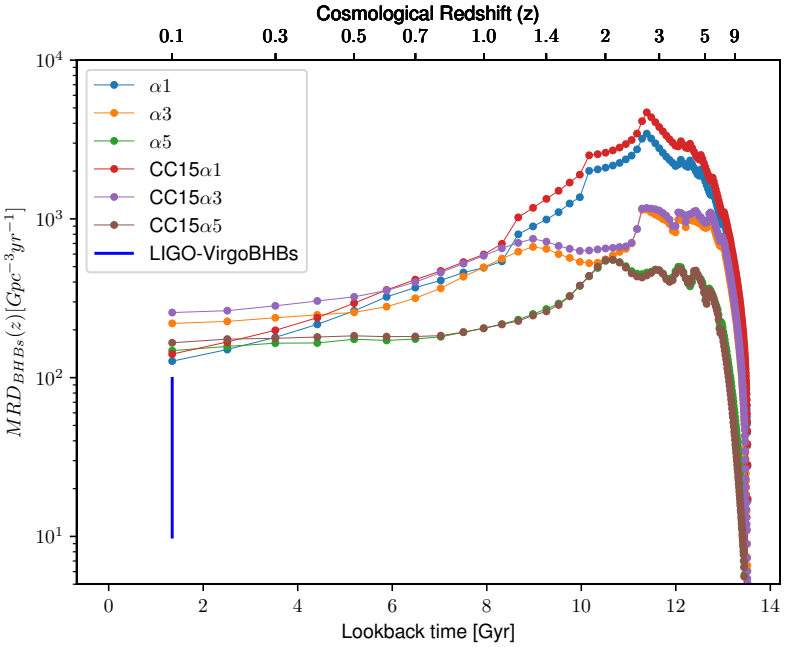

(b) BBHs - De Cia et al.,2018

Figure 6.2: The cosmic BBH MRD evaluated with Rafelski et al. (2012)(a) and De Cia et al. (2016) (b) metallicity evolution model, for the various population-synthesis prescriptions (see table 3.1). The BBH LIGO-Virgo confidence interval (blue vertical line) is shown as a comparison (see table 6.1) and is placed at redshift $z = 0.1$ for simplicity

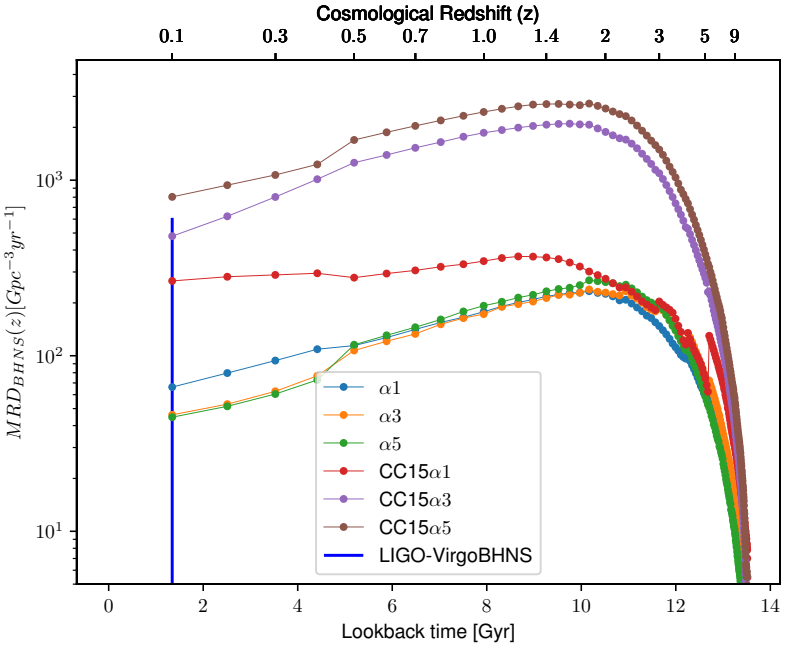

(a) BHNS - Rafelski et al.,2012

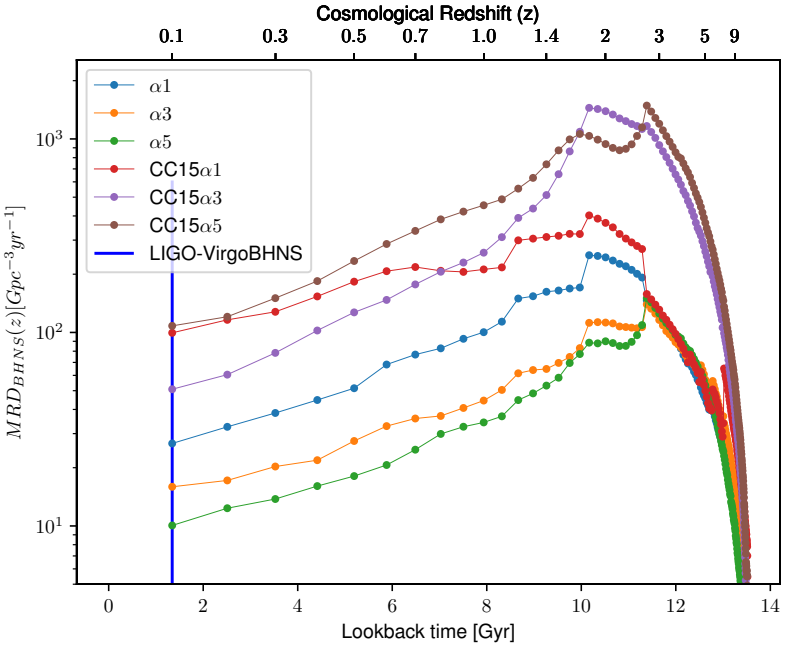

(b) BHNS - De Cia et al.,2018

Figure 6.3: The cosmic BHNS MRD evaluated with Rafelski et al. (2012)(a) and De Cia et al. (2016) (b) metallicity evolution model, for the various population-synthesis prescriptions (see table 3.1). The BHNS LIGO-Virgo upper level (blue vertical line) is shown as a comparison (see table 6.1) and it is placed at redshift $z = 0.1$ for simplicity

In figure 6.4(b), the Neijssel et al. (2019) predicts an higher BHNS merger rate density at redshift $z = 0.1$, but it is still under the upper limit of the LIGO-Virgo confidence interval. From redshift $z > 2$, the MRD tendencies are almost identical.

In figure 6.4(c), the MRD obtained with R2012 metallicity model is comparable with Neijssel's one, at redshift $z = 0.1$. In fact, N2019 state that the assumed metallicity distribution model has a similar shape to the metallicity distribution inferred by Rafelski et al. (2012). This is a crucial fact, because it proves that despite my model and N2019 one rely on different population-synthesis simulations, MRD evolution yield similar results once the metallicity distributions are comparable. However, both models are not consistent with BBH LIGO-Virgo credible interval. D2018 metallicity model provides so far the most reliable prediction of BBH merger rate density in the local Universe.

6.4.2 Mapelli & Giacobbo (2018)

The second work I chose for this comparison is Mapelli and Giacobbo (2018). They estimated the cosmic MRD of BBHs, DNSs and BHNSs by combining the results of the same population synthesis simulation presented in chapter 3, with the outputs of the Illustris-1 cosmological simulation (Vogelsberger et al., 2014). This method enables to account for the cosmic SFR density and for the metallicity evolution by means of a numerical simulation.

Figure 6.5(a) shows the DNS cosmic MRD obtained with the data-driven and numerical approaches. I notice that redshift $z = 0.6$ represents a turning point. Indeed, at $z > 0.6$ the full numerical model underestimates the merger number with respect to both data-provided cosmic evolution models. At $z < 0.6$ this trend is reversed.

In figure 6.5(b), the BHNS MRD is essentially the same for $z > 4$. At $z = 0.1$, the three MRD are compatible with the LIGO-Virgo upper level.

Illustris cosmological evolution predicts again a MRD which is placed between the values provided with the data-driven approach, regarding BBHs (see figure 6.5(c)). From $z > 4$, the MRD tendencies are again similar. D2018 provides so far the most reliable prediction of BBH cosmic MRD.

This comparison has been essential because it justifies the introduction of a data-driven model to compute the MRD across cosmic time. The cosmological evolution details that I lost adopting a data-driven approach do not prevent the evaluation oa a reliable cosmic MRD.

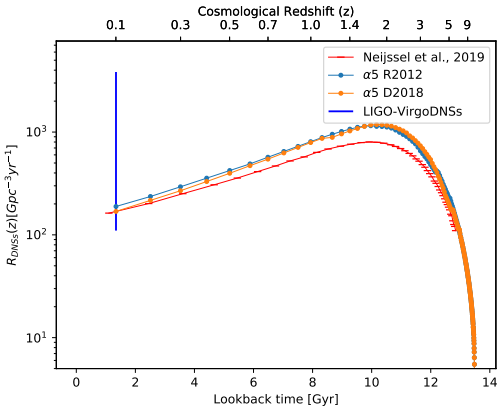

(a) DNS

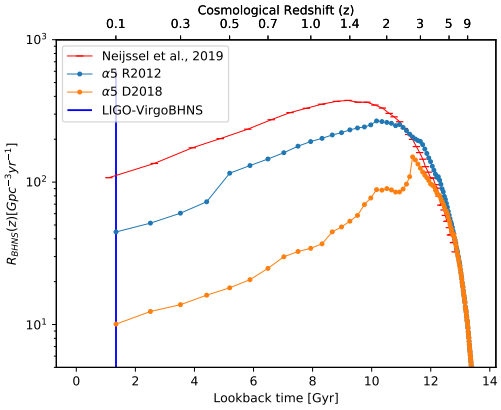

(b) BHNS

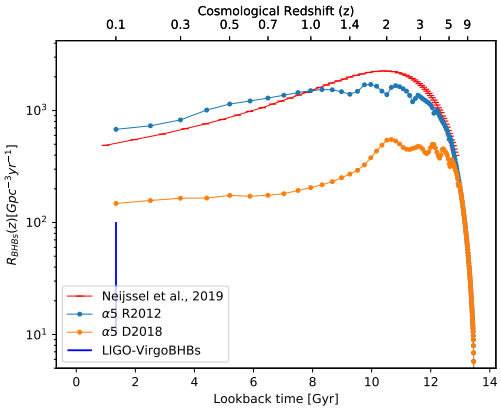

(c) BBH

Figure 6.4: Comparison between two data-driven models that evaluate the cosmic MRD. (Neijssel et al., 2019) (red line) included a spread in the metallicity evolution model. The comparison was made for DNSs (a), BHNS (b) and BBHs (c). LIGO-Virgo merger rates (blue vertical line) are placed to redshift $z = 0.1$ for simplicity

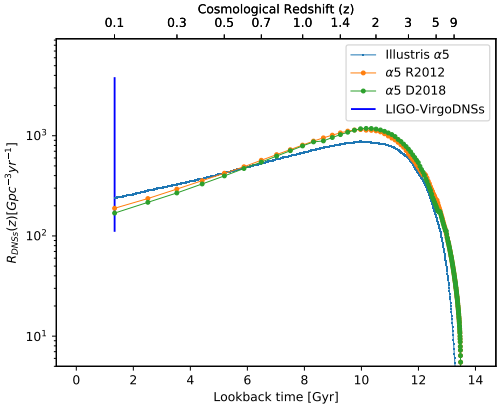

(a) DNSs

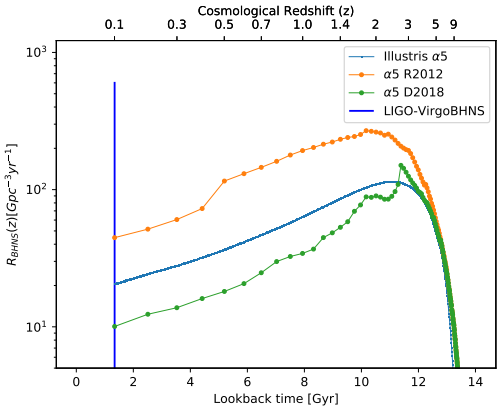

(b) BHNSs

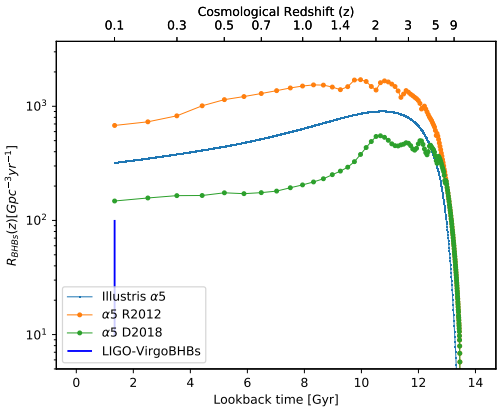

(c) BBHs

Figure 6.5: Comparison between the MRD across cosmic time obtained with a data-driven approach and with a full numerical simulation, where the cosmological evolution was obtained with Illustris (thin blue line) (Mapelli and Giacobbo, 2018). The comparison was made for DNSs (a), BHNS (b) and BBHs (c). LIGO-Virgo merger rates (blue vertical line) are placed to redshift $z = 0.1$ for simplicity

Chapter 7

Conclusions

In this thesis, I presented the theoretical background for the definition of a model that places population-synthesis results into a cosmological context, in order to find the cosmic MRD. MOBSE is the binary population-synthesis code that provided catalogues of merging DCOs. It explored the impact on DCO mergers of different binary evolution prescriptions, namely three different CE ejection efficiencies with high natal kicks ($\alpha 1$, $\alpha 3$ and $\alpha 5$) and low natal kicks (CC15$\alpha 1$, CC15$\alpha 3$ and CC15$\alpha 5$). The cosmological environment at different redshift was defined by data-driven functions that strongly affect the MRD.

The merging fraction of stellar-born DCOs increases, as the Madau and Dickinson (2014) SFRD increases at increasing redshift up to a peak which can be shifted with respect to $z \sim 2$, because of the delay time distributions. The MRD cosmic evolution cannot be model neglecting the SFRD. The progenitor metallicity plays also a fundamental role in determining the fate of a compact binary. Thus, I compared the cosmic MRD obtained with two different metallicity evolution models, Rafelski et al. (2012) and De Cia et al. (2018).

This thesis demonstrated that DNS cosmic MRD is strongly affected by binary evolution prescriptions, while the BBH cosmic MRD is mainly determined by the average metal content of the progenitor stars. The MRD is thus an essential parameter to be used to distinguish among various formation and evolution channels.

Predicting the number of merging BBHs in the local universe is still an open issue. Severe uncertainties still affect my model. For instance, measuring the cosmic metallicity evolution is extremely difficult as well as a lot of parameters that drive the population-synthesis simulations are still unconstrained. On the other hand, accurate estimates of the merging rate density can be provided by GW detections. The third LIGO-Virgo observing run is expected to terminate in April 2020. The improved detector sensitivity will provide several data which will shed light on these open issues.

7.1 Further developments

The model I presented in my thesis, can be promptly modified to achieve new interesting results. The changes can be both on the population-synthesis prescriptions and on the cosmological evolution.

In figure 6.1(a) and 6.1(b), I illustrated the impact of SN kicks on DNS cosmic MRD. Recently, Giacobbo and Mapelli (2019) developed a new model for natal kicks that is in agreement with observation of galactic pulsars. They run several MOBSE population-synthesis simulations characterised by various velocity distributions of natal kicks. It is now possible to evaluate the MRD across cosmic time of DNSs with these new kick prescriptions.

One of the key open questions of GW astrophysics is determining the contribution to MRD of isolated binary evolution and dynamical environment. Di Carlo et al. (2019) provided a catalogue of merging BBHs in young star clusters, with initial metallicity $Z = 0.002$. However, it is necessary to run other dynamical simulations with different initial metallicities. Indeed, it has been already assessed the impact of metallicity on cluster dynamics (Mapelli et al., 2013). Once these new data are available, in order to evaluate the MRD of dynamical evolved DCOs, is necessary to update the delay time distributions in equation 5.6, with the one obtained by dynamical simulations, leaving unchanged the SFRD and the metallicity evolution.

Furthermore, I can improve my model by adding a metallicity spread, which is necessary to take into account the physical fact that galaxies with different masses have different metallicities, although born in the same redshift bin, according to the mass-metallicity relation (Tremonti et al., 2004).

Another interesting development is the determination of the merger rate density per galaxy. Artale et al. (2019) combined, via a Monte Carlo method, CC15α5 merging DCO catalogue, with galaxy catalogues obtained with the cosmological hydrodynamical simulation EAGLE. They found that the MRD per galaxy strongly correlates with the stellar mass of the host galaxy and the galaxy SFR. These results were achieved by means of a numerical approach. My data-driven model can be thus extended to evaluate the MRD per galaxy, once a specific SFRD and a galaxy metallicity distribution is provided. Host galaxies must be characterised in order identify the most likely formation channels.

Appendices

Appendix A

Adopted cosmology

I assumed a standard spatially-flat 6-paramter ΛCDM cosmology. The cosmological parameters are provided by *Planck 2015*, Planck Collaboration et al. (2016), whose results rely on full-mission *Planck* observations of temperature and polarisation anisotropies of Cosmic Microwave Background (CMB). Table A.1 summarises some relevant parameters for this Thesis.
The third density parameter Ω_k measures the curvature of space and is defined by the following relation

$$\Omega_m + \Omega_\Lambda + \Omega_k = 1$$

In this thesis, it is considered equal to zero.

Hubble Constant	H_0	67.8 ± 0.9 km s^{-1} Mpc^{-1}
Hubble Time	t_{H_0}	14.4 ± 0.2 Gyr
Matter density parameter	Ω_m	0.308 ± 0.012
Reionization redshift	z_{re}	$8.8^{+1.7}_{-1.4}$

Table A.1: Cosmological parameters assumed in this thesis (Planck Collaboration et al., 2016).

Appendix B

Python script

```
#########################################################
# DCOs merging rate density as a function cosmological
# redshift. Carefully read README.txt before launching
# the code. It needs imput arguments
#########################################################

import time
start_time = time.time()
import numpy as np
import matplotlib.pyplot as plt
from astropy.cosmology import Planck15 as Planck
import astropy.units as u
import os
import sys



#Simulations form MOBSE
sim = ["A1" , "A3", "A5", "CC15A1", "CC15A3", "CC15A5"]

#Initial metallicities
Z = ["0.0002","0.0004","0.0008","0.0012","0.0016","0.002"
   ,"0.004","0.006","0.008","0.012","0.016","0.02"]
Z_list = [float(i) for i in Z]

#Redshift array
bin_z = 0.1
zMAX = 15
zMIN = -0.01
#from redshift Zmax to Zmin, i.e from firstly formed
   stars to nowadays
z_hist = np.arange(zMAX, zMIN, -bin_z)
```

```
#Lookback time array, used for the histogram of the delay
    times
bin_t1 = sorted(np.array(Planck.lookback_time(z_hist))
   *10**9) #in yrs
bin_t = np.insert(bin_t1, 0, 0) #beginning from zero

# INPUT: select the compact objects of which we perform
   the computations,
# it can be either BHBs or DNSs or BHNS
obj = sys.argv[1]

#Create the file where we will save the data, in our case
    it will be a matrix where
#the columns will be the different set of simulations and
    the rows the MRD as a function
#of redshift
os.system("rm data/output/MR_"+obj+"_"+metmod+".txt")  #-
   --->remove the previous file.dat
os.system("mkdir data/output")

#Define the matrix where we save our data
w = (len(sim), len(z_hist))
MR_z = np.zeros(w)

#INPUT: metallicity evolution models
metmod = sys.argv[2]
print(metmod)

def metz(z):
    if metmod == 'Raf2':#no intercept, i.e solar
       metallicity at redshift zero
        if z <= 1.5:
            M_H = -0.19*z
        else:
            M_H = -0.22*z
        Z_average = 0.02*10**M_H
    if metmod == 'Raf':
        if z <= 1.5:
            M_H = (-0.19)*z-0.74 #M_H stands for the
               ratio of metal content over gas
            #(i.e hydrogen) content, we do it in orther
               to compute the cosmic metallicity
            #as defined by Rafelski
        else:
            M_H = (-0.22)*z-0.66
        Z_average = 0.02*10**M_H
    elif metmod == 'LowestMet':
```

```
            if obj == 'DNSs':
                Z_average = 0.002
            else:
                Z_average = 0.0002
        elif metmod == 'HighestMet':
            Z_average = 0.02
        elif metmod == 'DeCia':
            Z_average =0.02*10**(-0.18-0.24*z)
        elif metmod == 'DeCia2':
            Z_average =0.02*10**(-0.24*z)
        return Z_average


#Loop over the simulations
for s in range(len(sim)):
    print(sim[s])
    #Load the table with the merger per unit mass
    [Zsim,rb,rn,rbn] = np.loadtxt('data/'+ sim[s] + '/
       table_merger_per_unit_mass.txt',
    skiprows=1,unpack=True)
    #Decide what objects
    if(obj == 'BHBs'):
        R_cor = rb
        objN = 1
    elif(obj == 'DNSs'):
        R_cor = rn
        objN = 0
    elif(obj == 'BHNS'):
        R_cor = rbn
        objN = 2

    w = (len(z_hist), len(z_hist))
    v = np.zeros(w) #it is a square matrix made up by
       zeros, it is used for
    #saving the histogram values
    i = 0 #this index runs on formation redshift
    NM = np.zeros(len(z_hist)) # = SFR*dt, at given
       formation redshift
    index = np.zeros(len(z_hist), dtype = int) #indicates
        the metallicity array index

    #Loop over the formation redshift
    for zf in z_hist:

        #Star formation rate at a given redshift
        SFR = 0.015*(1 + zf-bin_z)**(2.7)/(1+((1 + zf-
           bin_z)/2.9)**(5.6))
```

```
# Msun yr-1 Mpc-3

min_dt = Planck.lookback_time(zf)/u.Gyr*10**9 #In
    yr
max_dt = Planck.lookback_time(zf-bin_z)/u.Gyr
   *10**9 #In yr
dt =  min_dt - max_dt

#Number of solar masses per unit volume [at the
   end will be converted in Gpc^{-3}]
NM[i] = dt*SFR # Msun Mpc-3

Z_average = metz(zf)

#find the closest Z in my simulations
err = 100.
for met in Z_list:
    if err > np.abs(Z_average - met):
        err = np.abs(Z_average - met)
        index[i] = Z_list.index(met)

#Load the data about the delay time, once we
   chose the
#given metallicity at a given formation redshift
[ID,m1in,m2in,mrem1,mrem2,mrem,td,sep,ec] = np.
   loadtxt('data/'+ sim[s] +'/data_'
+obj+'_'+Z[index[i]]+'.txt',skiprows=1,unpack=
   True)

#Compute the histogram of the merger time
t_form = np.array(Planck.lookback_time(zf)/u.Gyr
   *10**9) #yrs
t_merg = t_form - td*10**9 #yrs
# t_merg must be positive! we fix the binning
dtSorted = sorted(t_merg, key=float)
#evaluate the histogram
[vv, base] = np.histogram(dtSorted, bins = bin_t)


# histogram counts must be reversed (at low
   indices, high redshift)
# and normilised
v[:,i]  = vv[::-1]/float(len(td))

i = i + 1 # this index runs on formation
   redshifts
```

```
            #I evaluate the merging rate as a function of
               redshift
            rate = 0
        for k in range(0,len(z_hist),1):#k selects the
           merging redshift
            rate = 0
            print('z merging = ', z_hist[k])
            for q in range(0, k + 1, 1): #k+1 in order to
               have diagonal values
                rate = rate + v[k,q]*NM[q]*R_cor[index[q]]
                # v[k,q] is the fraction of merging compact
                   object formed at redshift q
                # and merging at redshift k. q is always
                   smaller or equal than k . k = 0
                # corresponds to redshift z = Zmax, i.e. 15.
                   We need the number of compact
                # object per unit mass, that's the why we
                   need to multply it by R_cor which
                # is the total number of merging compact
                   objects per unit mass
            MR_z[s, k] = rate/(bin_t[len(z_hist)-k]-bin_t[len
               (z_hist)-k-1])*10**9 #Gpc^-3 yr^-1


#Save MR_z info in a file and make a plot
np.savetxt("MR_"+obj+"_"+metmod+".txt", np.transpose(np.
   asmatrix(MR_z)))
os.system("mv MR_"+obj+"_"+metmod+".txt data/output")

elapsed_time = time.time()-start_time
print('The code took  ', elapsed_time/60, 'minutes to run
   ')
```

Bibliography

Abbott, B. P., R. Abbott, T. D. Abbott, M. R. Abernathy, F. Acernese, K. Ackley, Adams, and et al.
2018. Prospects for observing and localizing gravitational-wave transients with Advanced LIGO, Advanced Virgo and KAGRA. *Living Reviews in Relativity*, 21(1):3.

Abbott, B. P., LIGO Scientific Collaboration, Virgo Collaboration, and et al.
2016. Astrophysical Implications of the Binary Black-hole Merger GW150914. *apjl*, 818(2):L22.

Artale, M. C., M. Mapelli, N. Giacobbo, N. B. Sabha, M. Spera, F. Santoliquido, and A. Bressan
2019. Host galaxies of merging compact objects: mass, star formation rate, metallicity, and colours. *mnras*, 487(2):1675–1688.

Baibhav, V., E. Berti, D. Gerosa, M. Mapelli, N. Giacobbo, Y. Bouffanais, and U. N. Di Carlo
2019. Gravitational-wave detection rates for compact binaries formed in isolation: LIGO/Virgo O3 and beyond. *arXiv e-prints*, P. arXiv:1906.04197.

Barrett, J. W., S. M. Gaebel, C. J. Neijssel, A. Vigna-Gómez, S. Stevenson, C. P. L. Berry, W. M. Farr, and I. Mandel
2018. Accuracy of inference on the physics of binary evolution from gravitational-wave observations. *mnras*, 477(4):4685–4695.

Belczynski, K., G. Wiktorowicz, C. L. Fryer, D. E. Holz, and V. Kalogera
2012. Missing Black Holes Unveil the Supernova Explosion Mechanism. *apj*, 757(1):91.

Claeys, J. S. W., O. R. Pols, R. G. Izzard, J. Vink, and F. W. M. Verbunt
2014. Theoretical uncertainties of the Type Ia supernova rate. *aap*, 563:A83.

De Cia, A., C. Ledoux, L. Mattsson, P. Petitjean, R. Srianand, I. Gavignaud, and E. B. Jenkins
2016. Dust-depletion sequences in damped Lyman-α absorbers. A unified picture from low-metallicity systems to the Galaxy. *aap*, 596:A97.

De Cia, A., C. Ledoux, P. Petitjean, and S. Savaglio
2018. The cosmic evolution of dust-corrected metallicity in the neutral gas. *aap*, 611:A76.

Di Carlo, U. N., N. Giacobbo, M. Mapelli, M. Pasquato, M. Spera, L. Wang, and F. Haardt
2019. Merging black holes in young star clusters. *mnras*, 487(2):2947–2960.

Dominik, M., K. Belczynski, C. Fryer, D. E. Holz, E. Berti, T. Bulik, I. Mand el, and R. O'Shaughnessy
2013. Double Compact Objects. II. Cosmological Merger Rates. *The Astrophysical Journal*, 779(1):72.

Eggleton, P. P.
1983. Aproximations to the radii of Roche lobes. *apj*, 268:368–369.

Fryer, C. L., K. Belczynski, G. Wiktorowicz, M. Dominik, V. Kalogera, and D. E. Holz
2012. Compact Remnant Mass Function: Dependence on the Explosion Mechanism and Metallicity. *The Astrophysical Journal*, 749(1):91.

Gallazzi, A., J. Brinchmann, S. Charlot, and S. D. M. White
2007. A census of the physical parameters of nearby galaxies. In *Stellar Populations as Building Blocks of Galaxies*, A. Vazdekis and R. Peletier, eds., volume 241 of *IAU Symposium*, Pp. 556–560.

Giacobbo, N. and M. Mapelli
2018. The progenitors of compact-object binaries: impact of metallicity, common envelope and natal kicks. *Monthly Notices of the Royal Astronomical Society*, 480(2):2011–2030.

Giacobbo, N. and M. Mapelli
2019. The impact of electron-capture supernovae on merging double neutron stars. *mnras*, 482(2):2234–2243.

Giacobbo, N., M. Mapelli, and M. Spera
2018a. Merging black hole binaries: the effects of progenitor's metallicity, mass-loss rate and Eddington factor. *mnras*, 474(3):2959–2974.

Giacobbo, N., M. Mapelli, and M. Spera
2018b. Unravelling the progenitors of merging black hole binaries. In *Gravitational-waves Science Symposium*, P. 27.

Hobbs, G., D. R. Lorimer, A. G. Lyne, and M. Kramer
2005. A statistical study of 233 pulsar proper motions. *mnras*, 360(3):974–992.

Hogg, D. W.
1999. Distance measures in cosmology. *arXiv e-prints*, Pp. astro–ph/9905116.

Hurley, J. R., C. A. Tout, and O. R. Pols
2002. Evolution of binary stars and the effect of tides on binary populations. *Monthly Notices of the Royal Astronomical Society*, 329(4):897–928.

Ivanova, N., S. Justham, X. Chen, O. De Marco, C. L. Fryer, E. Gaburov, H. Ge, E. Glebbeek, Z. Han, X. D. Li, G. Lu, T. Marsh, P. Podsiadlowski, A. Potter,

N. Soker, R. Taam, T. M. Tauris, E. P. J. van den Heuvel, and R. F. Webbink
2013. Common envelope evolution: where we stand and how we can move forward. *aapr*, 21:59.

Kroupa, P.
2001. On the variation of the initial mass function. *Monthly Notices of the Royal Astronomical Society*, 322(2):231–246.

Langer, N. and C. A. Norman
2006. On the Collapsar Model of Long Gamma-Ray Bursts:Constraints from Cosmic Metallicity Evolution. *apjl*, 638(2):L63–L66.

Littenberg, T. B., B. Farr, S. Coughlin, V. Kalogera, and D. E. Holz
2015. Neutron Stars versus Black Holes: Probing the Mass Gap with LIGO/Virgo. *apjl*, 807(2):L24.

Madau, P. and M. Dickinson
2014. Cosmic Star-Formation History. *Annual Review of Astronomy and Astrophysics*, 52:415–486.

Mapelli, M.
2018. Astrophysics of stellar black holes. *arXiv e-prints*, P. arXiv:1809.09130.

Mapelli, M. and N. Giacobbo
2018. The cosmic merger rate of neutron stars and black holes. *MNRAS*, 479(4):4391–4398.

Mapelli, M., N. Giacobbo, E. Ripamonti, and M. Spera
2017. The cosmic merger rate of stellar black hole binaries from the Illustris simulation. *Monthly Notices of the Royal Astronomical Society*, 472(2):2422–2435.

Mapelli, M., L. Zampieri, E. Ripamonti, and A. Bressan
2013. Dynamics of stellar black holes in young star clusters with different metallicities - I. Implications for X-ray binaries. *mnras*, 429(3):2298–2314.

Neijssel, C. J., A. Vigna-Gómez, S. Stevenson, J. W. Barrett, S. M. Gaebel, F. Broekgaarden, S. E. de Mink, D. Szécsi, S. Vinciguerra, and I. Mandel
2019. The effect of the metallicity-specific star formation history on double compact object mergers. *arXiv e-prints*, P. arXiv:1906.08136.

Panter, B., A. F. Heavens, and R. Jimenez
2004. The mass function of the stellar component of galaxies in the Sloan Digital Sky Survey. *mnras*, 355(3):764–768.

Peters, P. C.
1964. Gravitational Radiation and the Motion of Two Point Masses. *Physical Review*, 136(4B):1224–1232.

Planck Collaboration, P. A. R. Ade, and et al.
2016. Planck 2015 results. XIII. Cosmological parameters. *Astronomy and Astrophysics*, 594:A13.

Rafelski, M., M. Neeleman, M. Fumagalli, A. M. Wolfe, and J. X. Prochaska
2014. The Rapid Decline in Metallicity of Damped Lyα Systems at $z \sim 5$. *apjl*, 782(2):L29.

Rafelski, M., A. M. Wolfe, J. X. Prochaska, M. Neeleman, and A. J. Mendez
2012. Metallicity Evolution of Damped Lyα Systems Out to z ~5. *Apj*, 755(2):89.

Reitze, D., R. X. Adhikari, and et al.
2019. Cosmic Explorer: The U.S. Contribution to Gravitational-Wave Astronomy beyond LIGO. *arXiv e-prints*, P. arXiv:1907.04833.

Sana, H., S. Lacour, J. Le Bouquin, A. de Koter, C. Moni-Bidin, L. Muijres, O. Schnurr, and H. Zinnecker
2012. Sparse Aperture Masking of Massive Stars. In *Proceedings of a Scientific Meeting in Honor of Anthony F. J. Moffat*, L. Drissen, C. Robert, N. St-Louis, and A. F. J. Moffat, eds., volume 465 of *Astronomical Society of the Pacific Conference Series*, P. 363.

Schmidt, F. D.
2016. Dynamical Friction on Supersonic Gravitating and Non-Gravitating Spheres in a Gaseous Medium. *Master Thesis*.

Sobral, D., J. Matthee, B. Darvish, D. Schaerer, B. Mobasher, H. J. A. Röttgering, S. Santos, and S. Hemmati
2015. Evidence for PopIII-like Stellar Populations in the Most Luminous Lyman-α Emitters at the Epoch of Reionization: Spectroscopic Confirmation. *The Astrophysical Journal*, 808(2):139.

Spera, M. and M. Mapelli
2017. Very massive stars, pair-instability supernovae and intermediate-mass black holes with the sevn code. *mnras*, 470(4):4739–4749.

Spera, M., M. Mapelli, and A. Bressan
2015. The mass spectrum of compact remnants from the PARSEC stellar evolution tracks. *Monthly Notices of the Royal Astronomical Society*, 451(4):4086–4103.

The LIGO Scientific Collaboration, the Virgo Collaboration, and et al.
2018. GWTC-1: A Gravitational-Wave Transient Catalog of Compact Binary Mergers Observed by LIGO and Virgo during the First and Second Observing Runs. *arXiv*, P. arXiv:1811.12907.

Tremonti, C. A., T. M. Heckman, G. Kauffmann, J. Brinchmann, S. Charlot, S. D. M. White, M. Seibert, E. W. Peng, D. J. Schlegel, A. Uomoto, M. Fukugita, and J. Brinkmann
2004. The Origin of the Mass-Metallicity Relation: Insights from 53,000 Star-forming Galaxies in the Sloan Digital Sky Survey. *apj*, 613(2):898–913.

Vogelsberger, M., S. Genel, V. Springel, P. Torrey, D. Sijacki, D. Xu, G. Snyder, S. Bird, D. Nelson, and L. Hernquist
2014. Properties of galaxies reproduced by a hydrodynamic simulation. *nat*, 509(7499):177–182.

List of Figures

List of Tables

Acronyms

3G third generation.

BBH binary black hole.

BH black hole.

CCSNe core-collapse supernovae.

CE common envelope.

DCO double compact object.

DLAs damped Ly-α systems.

DNS double neutron star.

ECSNe electron-capture supernovae.

GW gravitational wave.

LVC LIGO-Virgo collaboration.

MRD merger rate density.

NS neutron star.

PISNe pair-instability supernovae.

RLOF Roche lobe overflow.

SFR star formation rate.

SN supernova.

WD white dwarf.

Acknowledgements
(in Italian)

Desidero ringraziare sentitamente la professoressa Mapelli. Il suo instancabile impegno ha reso possibile quanto realizzato in queste pagine. Sono orgoglioso di aver appreso i suoi fruttuosi insegnamenti, e non posso che essere contento di prolungare la nostra collaborazione. Voglio inoltre riservare un ringraziamento a tutte le colleghe e colleghi del gruppo di ricerca DemoBlack per la disponibilità e i preziosi consigli. Sono altrettanto riconoscente dello sforzo protratto dai miei genitori per elargire i mezzi necessari all'adempimento di questo ulteriore traguardo. Ogni mio successo non sarebbe stato realizzabile senza il loro supporto. Voglio ringraziare i miei nonni, i miei zii, i miei cugini, mia sorella Noemi e tutti coloro che si sono sempre interessati alla mia causa, informandosi, dandomi consigli, coraggio e stima. Si meritano un posto in questa lista anche Rafael, Federico, i ragazzi della SanPre, Bobo, le ragazze-Corrubbio e G. Moserle. Sono inoltre riconoscente verso i miei compagni di corso. Ringrazio gli astronomi-astronomi perché mi hanno subito inserito in un ambiente cordiale; e ringrazio anche gli astronomi-fisici con cui abbiamo passato del tempo felice: incontrarli è stato davvero bello! Voglio ringraziare anche lei: *la prima e l'ultima, il mio tutto*. La ringrazio per il costante supporto, per la tanta pazienza e per ricordarmi ogni giorno che quello che studio tanto non lo vedrà mai nessuno :)